Research Square

Preprints are preliminary reports that have not undergone peer review.
They should not be considered conclusive, used to inform clinical practice,
or referenced by the media as validated information.

Sharpening SST fronts have intensified eddy-induced turbulent heat fluxes in global mid-latitude oceans over the past three decades

Fangguo Zhai

gfzhai@ouc.edu.cn

1.Ocean University of China 2.Hebei Key Laboratory of Ocean Dynamics

Yikuan Liu

ocean university of China

Zizhou Liu

ocean university of China

Xiaojie Yu

ocean university of China

Cong Liu

Hainan Institute of Zhejiang University

Yanzhen Gu

State Key Laboratory of Ocean Sensing & Ocean College, Zhejiang University https://orcid.org/0000-0003-4616-867X

Peiliang Li

Zhejiang University

Article

Keywords:

Posted Date: June 2nd, 2026

DOI: https://doi.org/10.21203/rs.3.rs-9884337/v1

License: This work is licensed under a Creative Commons Attribution 4.0 International License.
Read Full License

Additional Declarations: There is **NO** Competing Interest.

Sharpening SST fronts have intensified eddy-induced turbulent heat fluxes in global mid-latitude oceans over the past three decades

Yikuan Liu[1], Fangguo Zhai[1,2], Zizhou Liu[1], Xiaojie Yu[3], Cong Liu[4], Yanzhen Gu[5], Peiliang Li[5]

1 State Key Laboratory of Physical Oceanography, College of Oceanic and Atmospheric Sciences, Ocean University of China, Qingdao, China

2 Hebei Key Laboratory of Ocean Dynamics, Resources and Environments, Qinhuangdao, China

3 Key Laboratory of Marine Environment and Ecology, College of Environmental Science and Engineering, Ocean University of China, Qingdao, China

4 Hainan Institute of Zhejiang University, Sanya, China

5 State Key Laboratory of Ocean Sensing & Ocean College, Zhejiang University, Zhoushan, China

Corresponding authors: Fangguo Zhai (gfzhai@ouc.edu.cn) & Xiaojie Yu (yxj@ouc.edu.cn)

Abstract

Mesoscale eddies profoundly modulate air–sea turbulent heat fluxes (THF). Their long-term trends and drivers under a changing climate remain uncertain. Using six high-resolution flux products, satellite SST datasets and a global eddy trajectory atlas, we isolate mesoscale thermodynamic footprints from the large-scale background. We reveal that eddy-induced THF is disproportionately concentrated in the mid-latitude SST fronts, especially in the western boundary currents and Antarctic Circumpolar Current, where eddies contribute 10–30% of climatological THF. These hotspots exhibit a robust, dataset-independent intensification, with decadal growth rates surging to 28–43% in the Gulf Stream, significantly outpacing the global mean (~20%). Linearized attribution indicates that this intensification is dominated by ocean-surface SST and humidity anomalies associated with sharpening of background SST gradients, rather than by enhanced eddy kinetic energy. Our results identify frontal sharpening as a key control on mesoscale air–sea heat exchange in a warming climate.

The ocean–atmosphere interface is a fundamental component of the Earth's climate system, where exchanges of momentum, heat, and moisture regulate a wide range of physical and dynamical processes[1–3]. Air-sea interactions, particularly THF—including latent and sensible heat exchange—mediate the transfer of thermal energy, thereby influencing SST distributions, convection, and large-scale climate phenomena[2,4–8]. Consequently, understanding the mechanisms and variability of air-sea heat fluxes is essential for accurately modeling and predicting climate dynamics[9,10].

Among diverse ocean dynamical processes, mesoscale eddies have been shown to exert a particularly strong influence on air–sea heat exchange[1,2,11]. These quasi-geostrophic[6], coherent rotating structures redistribute heat and salt, strongly shaping the spatiotemporal structure of the upper ocean[11,12]. Eddies generate SST anomalies primarily through vertical isopycnal displacements and horizontal stirring[13,14,15], which in turn alter air–sea temperature and humidity gradients, driving profound perturbations in THF[16,17]. Crucially, the magnitude of these eddy-induced air-sea interactions is highly spatially heterogeneous[18,19]. In mid-latitude regions characterized by sharp background SST fronts—such as the Antarctic Circumpolar Current (ACC) and the western boundary current extensions—intense baroclinic instabilities produce highly energetic eddies[19–22]. Within these localized SST peaks, the strong background thermodynamic gradients amplify eddy-induced SST anomalies, causing the eddy-induced THF to account for a disproportionately high percentage of the climatological mean fluxes.

Under a warming climate, global oceanic fronts are undergoing significant shifts and intensification[23,24]. However, how this intensification of background SST fronts alters the long-term trends of mesoscale air-sea interactions remains largely unexplored. While it is theoretically recognized that background gradients modulate eddy properties[11,15], a global-scale quantification of the long-term trends in eddy-induced THF, and the attribution of these trends to specific physical drivers (e.g., wind speed, transfer coefficients, or background SST gradients), is still lacking[9,17].

Addressing this gap requires robust, long-term observational records. Yet, considerable discrepancies exist among studies investigating eddy-induced THF across different

ocean regions, owing to variations in data products and eddy detection methodologies[25–27]. Furthermore, some datasets apply temporal or spatial smoothing that obscures high-frequency mesoscale variability[9]. These discrepancies illustrate that relying on a single dataset may introduce systematic biases when evaluating long-term trends in eddy-rich regions.

Therefore, to overcome the aforementioned observational uncertainties and uncover the underlying physical mechanisms, this study conducts a comprehensive global assessment of eddy-induced THF using an ensemble of six independent high-resolution air-sea flux datasets. By coupling a continuous, globally unified mesoscale eddy trajectory atlas with a rigorous linearized perturbation analysis thermodynamic decomposition framework[28], we systematically isolate the first-order impacts of mesoscale perturbations from the large-scale background climatology. Through this synthesized approach, we highlight the disproportionately dominant contribution of eddies to the total air-sea heat exchange at mid-latitude SST fronts and quantify their robust long-term intensification trends in these global hotspots. Ultimately, by definitively attributing these intensifying fluxes to the sharpening of background SST gradients, we establish a thermodynamically driven paradigm for decadal eddy–air-sea coupling.

Significant footprint of mesoscale eddies at mid-latitude oceanic fronts

To quantify the role of mesoscale eddies in global air-sea interactions, we evaluate the spatial distributions of the climatological mean THF and the eddy-induced THF anomalies (Fig. 1). The climatological THF exhibits extensive ocean-to-atmosphere heat loss, with strong heat exchange in large areas of low latitudes (over 120 W m^{-2}) and the magnitude decreases significantly beyond 45° (Fig. 1b). The highest THF occurs in the western boundary currents[29]. For instance, the climatological background heat release in the Kuroshio Extension (KE) and Gulf Stream (GS) typically exceeds 150 W m^{-2} (Fig. 1a, b). In contrast, the intensity of eddy-induced THF is largely confined to the western boundary currents and ACC regimes (Fig. 1c, d).

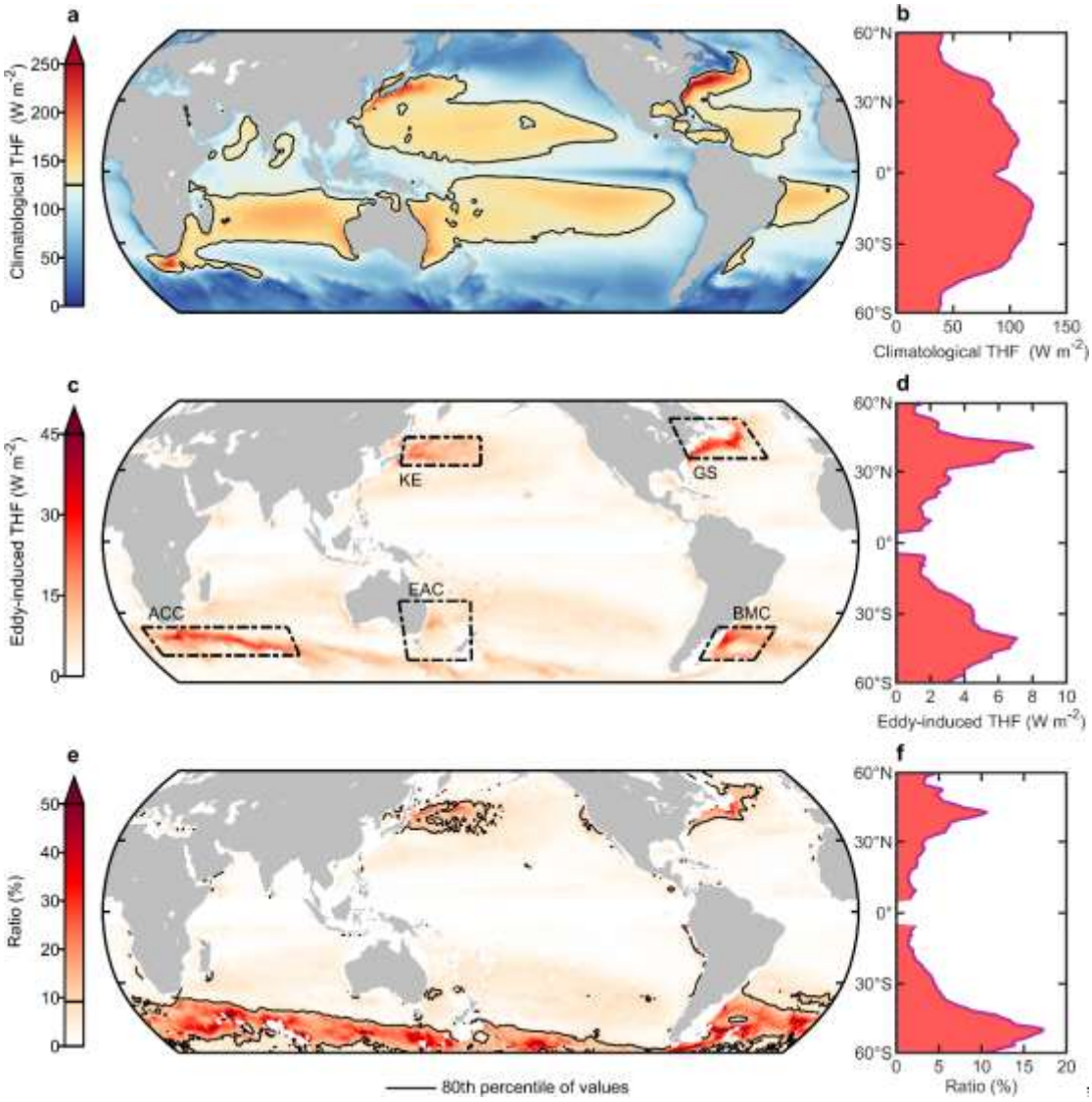


Fig. 1 | Climatological THF, eddy-induced THF intensity and the ratio of eddy-induced to climatological THF.

a, c, e, Spatial distribution of the climatological THF (**a**), eddy-induced THF anomalies (W m^{-2}) and the black dashed boxes delineate the study area (**c**) and the ratio of eddy-induced to climatological THF (**e**). **b, d, f**, Zonal-mean of the climatological THF (**b**), eddy-induced THF (**d**), ratio of eddy-induced THF to climatological THF (**f**). Solid black lines mark the 80th percentile contours.

Crucially, evaluating the relative contribution of eddies to the total heat exchange reveals a striking spatial disparity (Fig. 1e, f). While mesoscale eddies account for only a minor fraction (6.3%) of the climatological THF on a global average, their footprint becomes disproportionately dominant within mid-latitude SST fronts. As delineated by the top 20% thresholds (80th percentile contours, black lines in Fig. 1e), these global hotspots are explicitly anchored in the ACC, KE, GS, and the Brazil-Malvinas Confluence (BMC). To facilitate regional quantitative evaluations, we explicitly define

five highly energetic target frontal zones, with their precise geographical boundaries shown in Fig. 1c. Within these highly energetic, narrow frontal zones, the eddy-induced THF ratio rises sharply to 10–20%, and locally exceeds 30% in the core of the ACC. This stark quantitative contrast underscores that in these specific regions, eddies act not merely as high-frequency perturbations, but as the key modulators of regional air-sea thermal exchanges.

Eddy-induced heat fluxes in frontal zones

To further dissect the mechanisms driving these intense fluxes at mid-latitude fronts, we investigated the THF caused by anticyclonic eddies (AEs) and cyclonic eddies (CEs) respectively (Fig. 2). The composite spatial distributions exhibit a pronounced mirroring effect: AEs systematically enhance ocean-to-atmosphere heat loss (Fig. 2a), whereas CEs predominantly suppress background heat release (Fig. 2c). Spatially, the most extreme thermodynamic footprints are not uniformly distributed but are firmly anchored as elongated, narrow bands along the sharp SST gradients of the KE, GS, ACC, and the BMC, explicitly delineated by the 90th percentile contours. Zonal-mean profiles (Fig. 2b, d) further confirm this spatial confinement, peaking sharply at mid-latitudes between 9−12 W m^{-2} in both hemispheres.

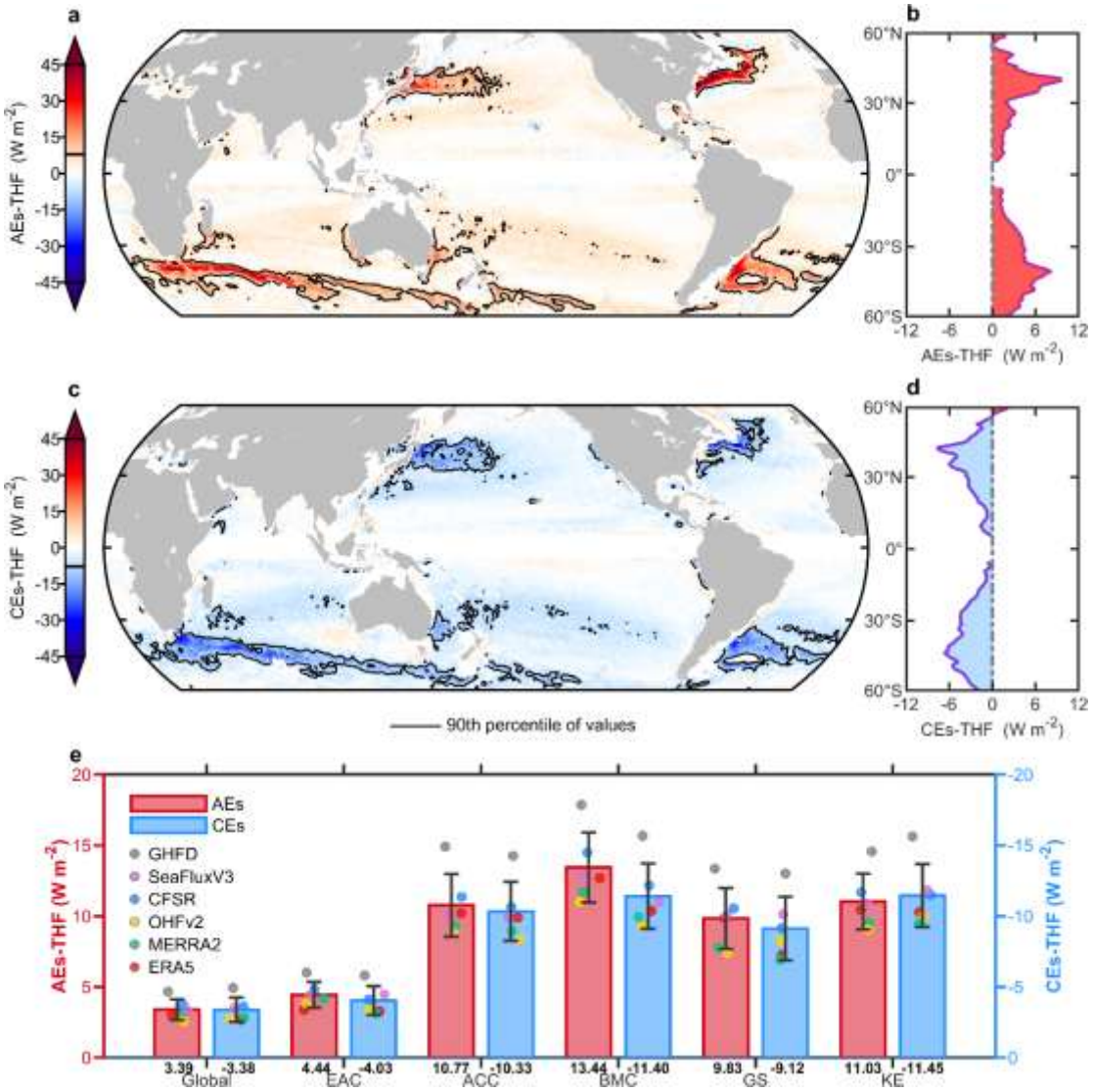


Fig. 2 | Spatial distribution of the eddy-induced THF and regional comparisons of the eddy-induced THF intensity between 1993 and 2018.

a, c, Global spatial distributions of composite THF anomalies (W m^{-2}) for AEs (**a**) and CEs (**c**). The black solid contours delineate the 90th percentile of the eddy-induced THF anomalies. **b, d**, Corresponding zonal-mean profiles of the THF anomalies for AEs (**b**) and CEs (**d**). **e,** Regional comparisons of the eddy-induced THF intensity between AEs (red bars) and CEs (blue bars) averaged over the global ocean and five highly energetic target regions: the East Australian Current (EAC), ACC, BMC, GS, and KE. The bar heights and error bars represent the ensemble mean and inter-product spread (one standard deviation), respectively, derived from six independent flux datasets. Colored scatter points denote the specific values estimated from each individual dataset (GHFD, SeaFluxV3, CFSR, OHFv2, MERRA2, and ERA5).

Quantitative evaluation across an ensemble of six independent flux datasets highlights the extreme regional disparity and thermodynamic asymmetry of these interactions (Fig. 2e). While the global mean eddy-induced THF magnitude remains modest at approximately 3.39 ± 0.74 W m^{-2} for AEs and -3.38 ± 0.85 W m^{-2} for CEs,

regional magnitudes in energetic frontal zones surge dramatically. In the Northern Hemisphere, the AE-induced THF in the GS and KE regions reaches 9.83 ± 2.16 W m^{-2} and 9.12 ± 2.25 W m^{-2}, respectively, exceeding the global average by more than a factor of 2.5. Similarly, the Southern Hemisphere hotspots exhibit intense anomalies, with the BMC contributing 13.44 ± 2.47 W m^{-2} for AEs and -11.40 ± 2.31 W m^{-2} for CEs.

This regional amplification is accompanied by a polarity-dependent asymmetry between AE and CE-induced THF responses, although the sign and magnitude of this asymmetry vary among frontal regions. AEs generally produce stronger THF anomalies than CEs over the global ocean and across most target regions, including the GS, ACC, BMC and EAC, with regional differences reaching 7.8% (0.71 W m^{-2}) in the GS, 4.3% (0.43 W m^{-2}) in the ACC, 17.9% (2.04 W m^{-2}) in the BMC and 10.0% (0.40 W m^{-2}) in the EAC. By contrast, the KE shows a slight reversal, where the magnitude of CE-induced THF exceeds the AE-induced THF by 3.7% (0.42 W m^{-2}). This regional exception does not alter the broader pattern that eddy polarity strongly modulates air–sea heat exchange, and the inter-product spread remains smaller than the regional anomaly signals in most frontal zones (Extended Data Fig. 1a–d).

Seasonal modulation of eddy-induced THF

Eddy-induced THF exhibits a pronounced seasonal modulation, with maximum amplitudes during local winter and minimum amplitudes during local summer (Fig. 3). In the Northern Hemisphere, the strongest responses occur in December, January and February (DJF) (Fig. 3g), particularly along the Kuroshio and Gulf Stream extensions, while the Southern Ocean signal maximizes in June, July and August (JJA) (Fig. 3c). This hemispheric phase reversal indicates that the seasonal cycle of eddy-induced THF is primarily controlled by the background atmospheric state: stronger wintertime winds, larger sea–air temperature and humidity disequilibria, and reduced boundary-layer stability, which are most conducive to air-sea transfer during local winter.[9,16,17].

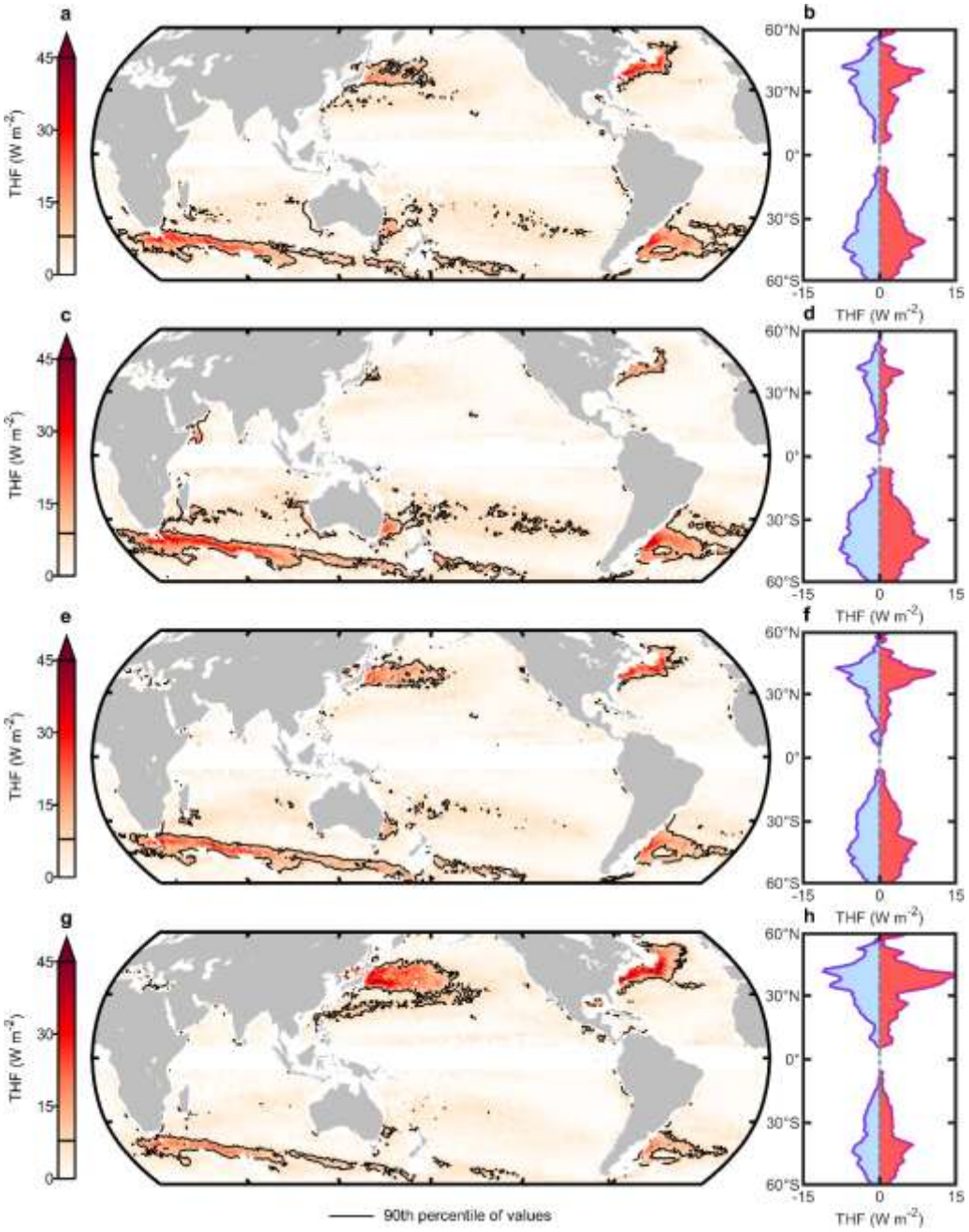


Fig. 3 | Seasonal variability in eddy-induced THF intensity between 1993 and 2018. **a**, **c**, **e**, **g**, seasonal mean eddy-induced THF intensity in MAM, JJA, SON and DJF. **b**, **d**, **f**, **h**, zonal-mean THF induced by eddies, red shading based on AEs and blue shading based on CEs. The black solid contours delineate the 90th percentile of the absolute eddy-induced THF anomalies.

Despite this strong seasonal modulation, the polarity-dependent asymmetry remains robust throughout the year. The zonal mean profiles (Fig. 3b,d,f,h) reveal that AEs consistently trigger stronger heat flux anomalies than CEs across all basins and seasons by approximately 20% (see Extended Data Fig. 2 for the detailed monthly THF intensity). This asymmetry is consistent with the nonlinear thermodynamic and

boundary-layer responses to SST anomalies: warm eddies enhance sea–air humidity disequilibrium and destabilize the marine atmospheric boundary layer, whereas cold eddies tend to stabilize the boundary layer and damp turbulent exchange[9,30,31]. Thus, the seasonal cycle modulates the magnitude of eddy-induced THF, but does not alter the fundamental AE-CE asymmetry.

Long-term intensification of eddy-induced THF in frontal zones

Building on the spatial dominance of eddy-induced fluxes, we further evaluate their long-term temporal evolution across the global ocean (Fig. 4). The spatial distribution of the decadal trends reveals a striking intensification of eddy-mediated thermodynamic feedbacks. Specifically, the THF induced by AEs exhibits widespread positive trends (Fig. 4a, b), indicating an accelerated heat release to the atmosphere, while that induced by CEs demonstrates enhanced negative trends (Fig. 4c, d), signifying an increasing suppression of background oceanic heat loss.

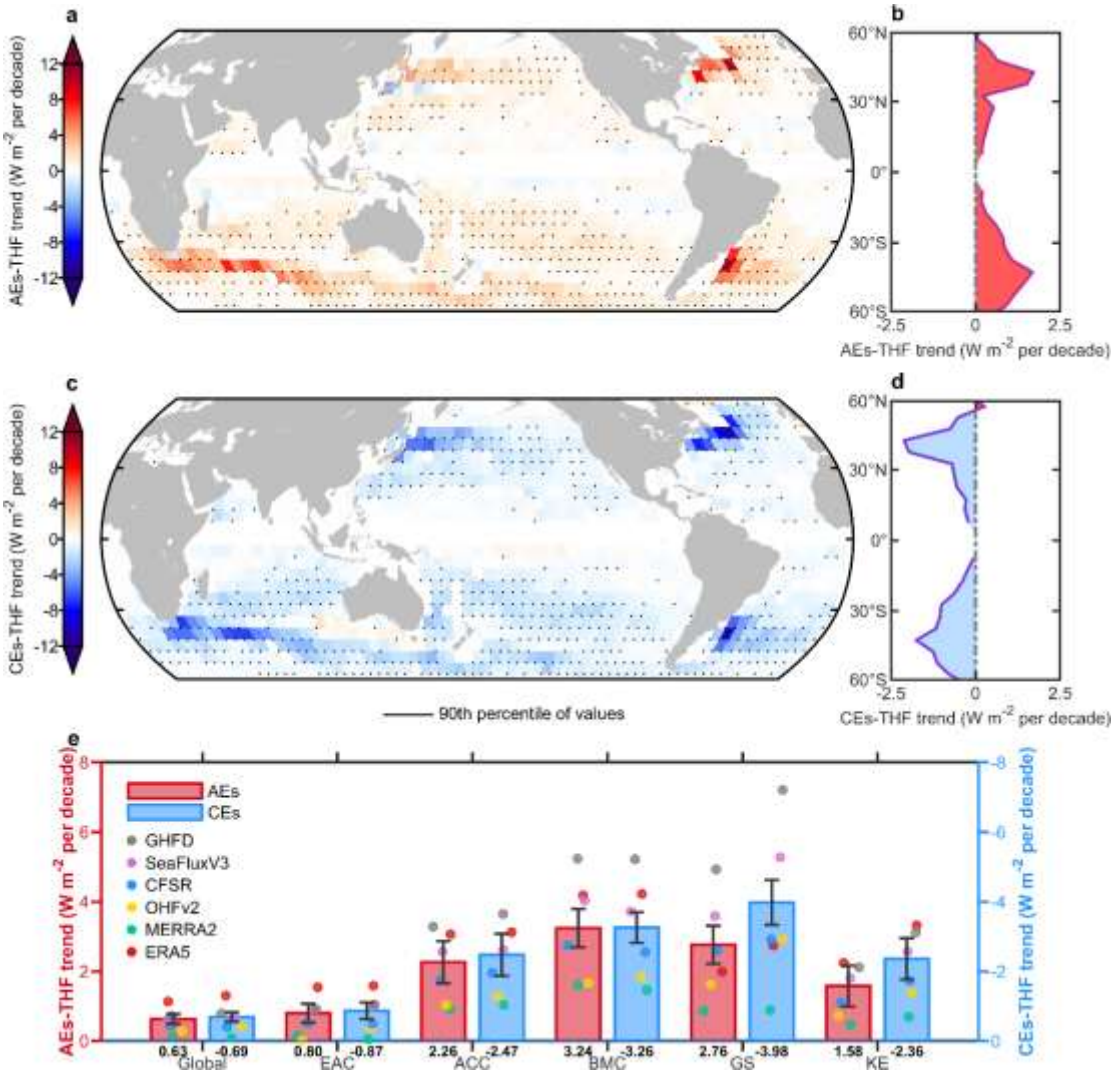


Fig. 4 | Long-term trend in eddy-induced THF and regional comparisons of the eddy-induced THF trend between 1993 and 2018.

a, c, Global spatial distributions of decadal trends in eddy-induced THF anomalies (W m^{-2} per decade) for anticyclonic eddies (**a**) and cyclonic eddies (**c**). Black stippling denotes regions where the decadal trends are statistically significant at the 95% confidence level, based on the Mann–Kendall test. **b, d**, Corresponding zonal mean profiles of the decadal THF trends for AEs (**b**) and CEs (**d**). **e**, Regional comparisons of the eddy-induced THF decadal trends for AEs (red bars) and CEs (blue bars) averaged over the global ocean and five highly energetic target regions. The bar heights represent the ensemble mean trends estimated using the Theil–Sen method. Error bars denote the 90% confidence intervals associated with the trend estimates. Colored scatter points represent the specific decadal trend values derived from each of the six independent flux datasets (GHFD, SeaFluxV3, CFSR, OHFv2, MERRA2, and ERA5).

However, these intensifying trends are spatially heterogeneous. Grid cells displaying statistically significant trends are concentrated primarily along dynamically active mid-latitude SST fronts, where the climatological eddy-induced THF is also strongest. A regional ensemble analysis further quantifies this localized amplification (Fig. 4e).

Relative to the climatological eddy-induced THF intensity, the global mean increase remains moderate, reaching 18.7% per decade for AEs (0.63 $\pm$ 0.14 W m^{-2} per decade) and 20.5% per decade for CEs (0.69 $\pm$ 0.14 W m^{-2} per decade in magnitude). In contrast, the major frontal zones exhibit much stronger relative intensification, with the corresponding interannual time series shown in Extended Data Fig. 3.

In the Northern Hemisphere western boundary currents, the GS and KE exhibit profound eddy THF intensification. In the GS, AE-induced THF increases by 28.1% (2.76 $\pm$ 0.55 W m^{-2} per decade), while the magnitude of CE-induced THF increases by 43.6% per decade (3.98 $\pm$ 0.64 W m^{-2} per decade). Similarly, in the KE, AE and CE-induced THF intensities increase by 14.3% (1.58 $\pm$ 0.59W m^{-2} per decade) and 20.6% (2.36 $\pm$ 0.59 W m^{-2} per decade), respectively. In the Southern Hemisphere, the BMC and ACC also exhibit robust intensification: AE-induced THF increases by 24.1% (3.24 $\pm$ 0.55 W m^{-2} per decade) and 21.0% (2.26 $\pm$ 0.61 W m^{-2} per decade), respectively, whereas CE-induced THF suppression strengthens by 28.6% (3.26 $\pm$ 0.44 W m^{-2} per decade) and 24.0% (2.47 $\pm$ 0.61 W m^{-2} per decade), respectively.

The polarity dependence of these trends is also regionally variable. In most target regions, the magnitude of CE-induced suppression intensifies faster than the AE-induced enhancement. For example, in the GS, CE-induced THF suppression increases 15 percentage points faster than AE-induced heat release, corresponding to an absolute trend difference of 1.22 W m^{-2} per decade. Nevertheless, the 90% confidence intervals and the individual product estimates indicate that the intensification of eddy-induced THF in major frontal zones is a robust, dataset-independent feature, despite inter-product spread among the six flux products (Extended Data Fig. 1e–h).

Oceanic surface anomalies dictate the THF intensification

To elucidate the physical drivers underpinning the accelerated eddy–air-sea coupling, we perform a linearized thermodynamic attribution analysis of the THF (see Methods for further details). This framework partitions the total eddy-induced THF trends into the thermodynamic term ($\mathrm{THF}'_{\mathrm{thermo}}$), the wind-driven term ($\mathrm{THF}'_{\mathrm{wind}}$), the turbulent-transfer coefficient term ($\mathrm{THF}'_{\mathrm{TC}}$), and higher-order residuals (RES). Spatial distributions of the climatological mean and decadal trends for these components

(Extended Data Figs. 4 and 5) reveal that the patterns and magnitudes of the total intensification are almost entirely reproduced by the $\mathrm{THF}'_{\mathrm{thermo}}$, which represents the robust mesoscale sea–air interface gradients acting under the modulation of background wind conditions.

To precisely quantify and pinpoint the origin of this gradient-driven intensification, we further isolate $\mathrm{THF}'_{\mathrm{thermo}}$ into oceanic surface term ($\mathrm{THF}'_{\mathrm{ocean}}$) and atmospheric term ($\mathrm{THF}'_{\mathrm{atmos}}$) (Fig. 5). The oceanic surface term represents the thermodynamic forcing originating from SST and sea surface saturation specific humidity anomalies, while the atmosphere term reflects adjustments in near-surface air temperature and specific humidity. Regional statistical quantification based on the composite mean of individual eddies provides evidence for a striking ocean-atmosphere asymmetry (Fig. 5a, b). The oceanic surface term overwhelmingly dictates both the climatological mean and the overarching intensification trends across all mid-latitude ocean fronts. For instance, within the GS and KE regions, $\mathrm{THF}'_{\mathrm{ocean}}$ accounts for 91.7% and 87.5% of the total decadal intensification for AEs, contributing 3.13 and 1.46 W m^{-2} per decade, respectively (Fig. 5c, d).

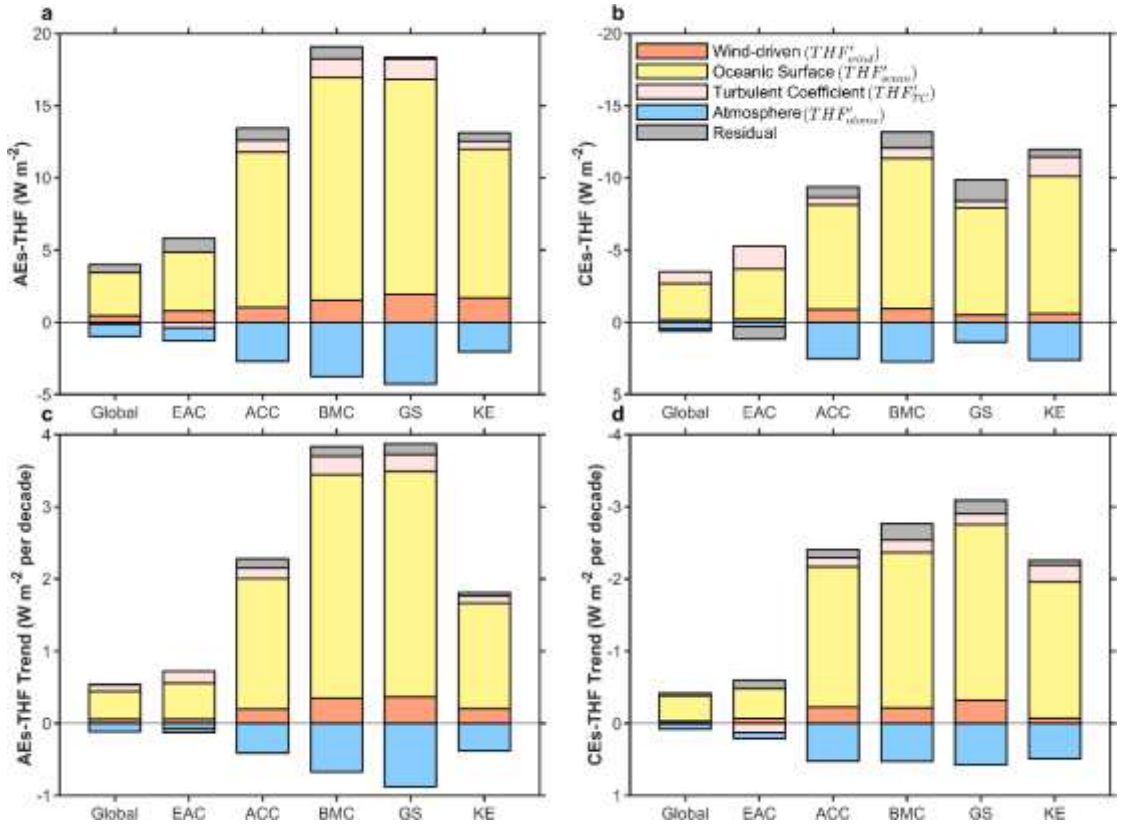


Fig. 5 | Quantitative regional attribution of eddy-induced THF and its decadal trends.

a, b, Regional integration of the climatological mean contributions (W m^{-2}) to the eddy-induced THF, decomposed into oceanic surface, atmosphere, turbulent-transfer coefficient and residual terms for both AEs (**a**) and CEs (**b**). The analysis is presented for the global ocean and the five key frontal zones (KE, GS, ACC, BMC, and EAC). **c, d**, Corresponding regional quantification of the contributions to the decadal trends (W m^{-2} per decade).

In stark contrast, the THF'_{atmos} consistently exhibits a negative contribution to the intensification trends, signifying that the atmospheric boundary layer acts as a passive respondent that tends to damp the ocean-driven anomalies rather than driving them. Furthermore, the combined contributions from THF'_{wind}, THF'_{TC} and RES exhibit near-zero long-term trends (Extended Data Fig. 5). This attribution confirms that the robust intensification of eddy-induced THF is unlikely to be explained by atmospheric circulation shifts or non-linear noise, but is fundamentally an ocean-driven thermodynamic process. The dominant contribution of the oceanic surface term traces the root cause of the amplified air–sea coupling back to the sharpening of background SST gradients, which provide an enhanced thermodynamic reservoir for mesoscale perturbations.

Thermodynamic intensification overshadows dynamic eddy kinetic energy variations

Ultimately, the magnitude of eddy-induced SST anomalies is governed by the stirring of large-scale background SST gradients by mesoscale velocity fields[33–35]. Independent estimates from OISST and ESA SST show that the eddy-induced SST anomalies have increased within major mid-latitude frontal zones particularly (Extended Data Fig. 6). The intensification of eddy-induced THF is primarily driven by SST anomalies (Fig. 5), we need to unravel the specific physical mechanisms driving SST intensification. To address this, we compare the climatology and decadal trends of the background SST gradients and eddy kinetic energy (EKE)[6,7] (Fig. 6).

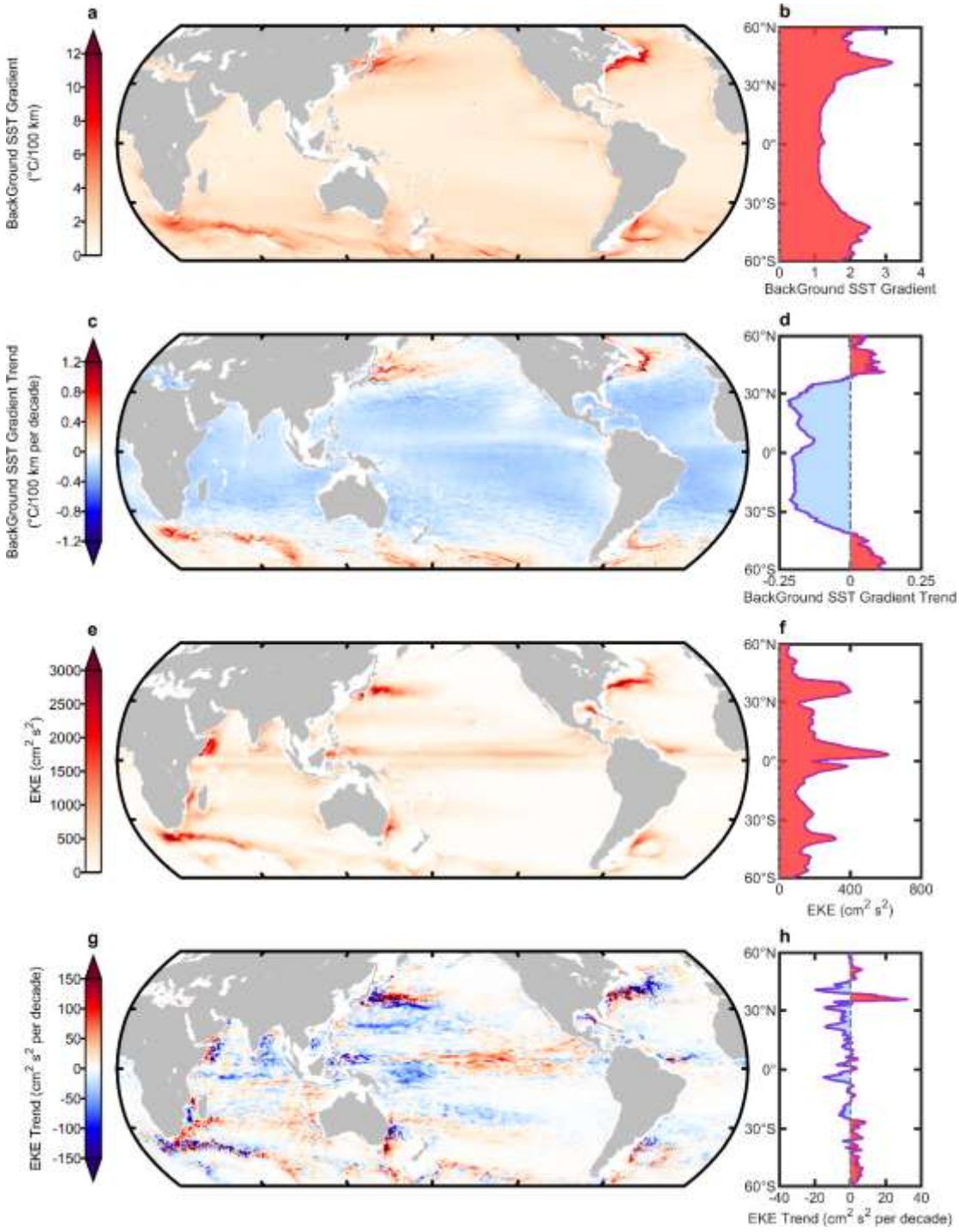


Fig. 6 | Mean SST gradient magnitude, SST gradient magnitude trends, mean surface EKE and surface EKE trend between 1993 and 2018.

a, **b**, Global spatial distribution (**a**) and the corresponding zonal mean profile (**b**) of the climatological background SST gradient (°C/100 km). **c**, **d**, Global spatial distribution (**c**) and the zonal mean profile (**d**) of the decadal trend in the background SST gradient (°C/100 km per decade). Positive trends (red shading) indicate a widespread intensifying, or sharpening, of the background thermal fronts. **e**, **f**, Global spatial distribution (**e**) and the corresponding zonal mean profile (**f**) of the climatological EKE ($cm^2\ s^{-2}$), highlighting the highly energetic nature of western boundary currents and the

Antarctic Circumpolar Current. **g**, **h**, Global spatial distribution (**g**) and the zonal mean profile (**h**) of the decadal trend in EKE ($cm^2\ s^{-2}$ per decade).

We used ESA SST to calculate the background sea surface temperature gradient (Fig. 6a, b), and its spatial distribution closely matches the identified THF hotspots, as well as the results calculated using OISST (Extended Data Fig. 7). Crucially, the decadal trend of the SST gradient (Fig. 6c, d) reveals a widespread, systematic intensification across almost all mid-latitude frontal zones in both hemispheres. The ACC, GS, KE, and BMC regions exhibit prominent positive trends, indicating that these background fronts have become significantly sharper over the past decades[33]. In stark contrast, the high-value region of eddy kinetic energy is mainly concentrated at the western boundary flow axis (Fig. 6e, f), the decadal trends of EKE (Fig. 6g, h) display high spatial heterogeneity, with alternating bands of strengthening and weakening signals. The absence of a uniform global EKE intensification implies that changes in the dynamic vigor of the eddies alone cannot account for the widespread and robust strengthening of eddy-induced THF observed across all targeted fronts. Object-based eddy statistics further indicate that trends in eddy amplitude, radius and occurrence frequency are spatially heterogeneous and do not coherently match the widespread intensification of eddy-induced SST and THF anomalies (Extended Data Fig. 8). To further remove the direct influence of eddy intensity, we normalized the eddy-induced SST anomalies by eddy amplitude. The amplitude-normalized SST response remains strongest in major mid-latitude frontal zones and exhibits robust decadal strengthening in both OISST and ESA SST (Extended Data Fig. 9). These results demonstrate that the enhanced mesoscale SST and THF responses are not simply a consequence of stronger, larger or more frequent eddies, but reflect an increased thermodynamic sensitivity of eddies to sharpened background SST fronts.

Discussion

Our results point to a background-state control on mesoscale air–sea thermal coupling. Rather than treating eddy-induced THF anomalies as a direct consequence of eddy dynamical intensity alone[35], the analyses reveal that their decadal evolution is strongly conditioned by the evolving thermal structure of mid-latitude ocean fronts[7]. This

mechanism can be conceptualized as a thermodynamic amplification of mesoscale eddy imprints by the background frontal state (Extended Data Fig. 10). Under a weak frontal background, eddies detached from the frontal current encounter relatively small cross-frontal SST contrasts and therefore induce only weak SST anomalies and limited perturbations in sea–air temperature and humidity disequilibrium. In contrast, under a sharpened SST front, comparable eddy perturbations act on a stronger background thermal gradient: AEs generate larger warm SST anomalies and enhanced upward turbulent heat fluxes, whereas CEs generate stronger cold SST anomalies and a greater suppression of ocean-to-atmosphere heat release. In this framework, the changing background thermal state acts as a gain factor that amplifies the surface expression of mesoscale eddies, thereby linking large-scale frontal sharpening to intensified mesoscale air–sea heat exchange.

The ubiquitous sharpening of these mid-latitude SST fronts necessitates a broader perspective linked to large-scale climate forcing[23,36]. The widespread sharpening of mid-latitude SST fronts may reflect a combination of long-term climate forcing, basin-scale circulation adjustments and regional frontal displacement or compression. Strengthening or poleward shifts of westerly winds, changes in western boundary current extensions and shifts in the ACC can alter frontal positions and cross-frontal thermal gradients[37,38]. It is precisely these macro-climate shifts that provide an increasingly potent thermodynamic reservoir, effectively "fueling" the mesoscale eddies to release amplified heat fluxes into the atmosphere[7,17].

These findings present critical implications for the projection of future climate trajectories. Current generation Global Climate Models often employ coarse spatial resolutions that struggle to accurately simulate sharp, localized SST gradients and explicitly resolve the associated mesoscale eddy field. Consequently, they may systematically underestimate the intensifying mesoscale air-sea feedbacks at mid-latitude fronts. Without transitioning towards high-resolution, eddy-resolving coupled models, we risk misrepresenting the long-term energy budget of the Earth's climate system. Furthermore, while integrating an ensemble of high-resolution products—including ERA5, MERRA-2, and CMEMS altimetry—effectively mitigates systematic

biases inherent to single datasets, our flux estimations fundamentally rely on bulk aerodynamic parameterizations. Future investigations should incorporate continuous subsurface observational networks (e.g., Argo floats) to explore how changes in mixed-layer depths and interior baroclinic instabilities synergistically modulate these surface thermodynamic signals.

Methods

Air-sea flux ensemble and background fields

To robustly quantify eddy-induced THF anomalies and mitigate the systematic uncertainties inherent to individual parameterizations, we employ an ensemble of six independent air-sea flux datasets: ERA5, CFSR, MERRA-2, GHFD, SeaFluxV3, and OHFv2. Utilizing a multi-product ensemble is crucial for isolating robust mesoscale thermodynamic signals from inter-product spread. To accurately resolve the large-scale background thermal state and its long-term gradients, daily high-resolution SST fields were derived from the ESA SST CCI and C3S reprocessed sea surface temperature analyses (commonly built upon the OSTIA system). Furthermore, to evaluate the dynamic modulation and kinetic energy of the mesoscale eddy field, daily geostrophic velocity anomalies were obtained from the Global Ocean Gridded L4 Sea Surface Heights and Derived Variables reprocessed product, provided by the Copernicus Marine Environment Monitoring Service (CMEMS).

Construction of the continuous mesoscale eddy trajectory dataset

The identification and tracking of mesoscale eddies were based on the Mesoscale Eddy Trajectory Atlas (META) produced by AVISO/CLS. To seamlessly cover our entire study period and assess long-term decadal trends, we constructed a continuous, globally unified eddy trajectory dataset spanning from January 1, 1993, to December 31, 2024. This was achieved by splicing two distinct META versions: the high-quality Delayed-Time all-satellite product (META3.2 DT allsat), which covers the period from January 1993 to early February 2022, and the Near-Real-Time experimental product (META3.2exp NRT), which provides the subsequent tracking data. Overlapping periods were carefully cross-validated to ensure the temporal consistency of eddy polarity, radius, and amplitude variations across the transition interface.

Identification of Eddy Signature

To robustly isolate mesoscale eddy signals from the complex, multi-scale spectrum of air-sea interactions, we applied a rigorous sequential spatiotemporal filtering procedure to all gridded SST and THF datasets. First, to mitigate the influence of synoptic atmospheric noise and high-frequency fluctuations unrelated to eddy dynamics, a 15-

day Lanczos low-pass filter was applied to the time series at each spatial grid point. Subsequently, to extract the mesoscale perturbations from the large-scale climatological background, a two-dimensional spatial high-pass filter, implemented via a Gaussian smoothing kernel with a 6° × 6° footprint, was applied to the temporally filtered fields. This sequential protocol effectively yields the anomaly fields that strictly represent thermodynamic variability operating at mesoscales[18,39]. Concurrently, to ensure the reliability of our composite and thermodynamic attribution analyses, we applied stringent objective criteria to the continuous eddy trajectory atlas. To avoid the complexities of coastal boundary interactions and transient noise, we focused exclusively on coherent, persistent, open-ocean eddies. Specifically, individual eddies were retained for analysis only if they satisfied all the following conditions: originating and propagating over deep ocean regions with bathymetry exceeding 1000 m and maintaining a continuous lifespan of more than 28 days. The composite analysis of mesoscale thermal footprints was subsequently performed by co-locating the filtered SST and THF anomaly fields onto the dynamic centers of these robust, long-lived eddies.

Eddy compositing and gridded trend estimation

To quantify the intensity of THF and SST anomalies induced by individual eddies, we performed an eddy composite analysis for each eddy snapshot. For a given eddy snapshot, filtered anomaly fields were interpolated onto an eddy coordinate system normalized by the eddy radius, and the eddy-induced anomaly intensity was defined as the mean anomaly within one eddy radius.

The resulting eddy-level anomaly intensities were subsequently mapped back to geographical grids according to the longitude and latitude of the corresponding eddy centroids. For climatological analyses, the eddy anomaly intensities were binned into 1° × 1° grid cells, whereas for trend analyses they were binned into 5° × 5° grid cells to improve the robustness of long-term estimates. Within each grid cell, eddy-level anomaly intensities were aggregated by month or by year, depending on the specific analysis, to construct monthly or annual time series representing the mean eddy-induced anomaly intensity in that grid cell. Climatological maps were obtained by

418 averaging the grid-cell time series over the full analysis period.

419 **Linearized Decomposition of Mesoscale turbulent Heat Fluxes**

420 While the robust intensification trends are validated using a multi-product ensemble,
421 the linearized physical decomposition is conducted exclusively using the CFSR
422 dataset[28]. CFSR is uniquely suited for this mechanistic attribution because it provides
423 explicitly archived, high-frequency diagnostic outputs for the turbulent transfer
424 coefficients (c_h and c_e). This allows for a mathematically closed and physically
425 consistent decomposition of the bulk formulas, avoiding the extraneous uncertainties
426 and biases introduced by offline parameterization schemes or the assumption of
427 constant coefficients required for other reanalysis products.

428 To quantify the relative contributions of key physical variables to mesoscale air-sea
429 heat flux anomalies and their decadal trends, we employ a methodology based on a
430 linearized decomposition of the turbulent heat flux bulk aerodynamic formulas. The
431 total THF, comprising sensible and latent heat fluxes, is fundamentally governed by
432 surface wind speed (U), the sea-air temperature difference ($T_s - T_a$), the sea-air specific
433 humidity difference ($q_s - q_a$), and the turbulent transfer coefficients. Here, T_s and T_a
434 denote the SST and 2-meter air temperature, while q_s and q_a represent the saturated
435 specific humidity at the ocean surface and 2-meter specific humidity, respectively. Note
436 that q_s is intrinsically tied to SST via the Clausius-Clapeyron relation.

437 Each variable X is decomposed into a large-scale background mean state ($\overline{X}$) and a
438 mesoscale perturbation (X'), separated via the spatiotemporal filtering described above.
439 Applying a first-order Taylor series expansion, the total mesoscale THF anomaly (THF')
440 can be linearly decomposed as:

441 $$THF' \approx THF'_{thermo} + THF'_{wind} + THF'_{TC} + RES \quad (1)$$

442 To directly align with the mechanistic attribution presented in our results, we further
443 partition the thermodynamic term (THF'_{thermo})—which represents fluxes driven by
444 mesoscale perturbations in the sea-air interface thermal and moisture disequilibrium—
445 into distinct oceanic and atmospheric components:

446 1. Oceanic Surface Term (THF'_{ocean}):

$$\mathrm{THF}'_{\mathrm{ocean}} = \rho_a \overline{U}(c_p \overline{c_h} T'_s + L_v \overline{c_e} q'_s) \quad (2)$$

This term isolates the active thermodynamic forcing originating exclusively from the ocean surface, driven by mesoscale anomalies in SST and the associated saturation specific humidity.

2. Atmospheric Term ($\mathrm{THF}'_{\mathrm{atmos}}$):

$$\mathrm{THF}'_{\mathrm{atmos}} = -\rho_a \overline{U}(c_p \overline{c_h} T'_a + L_v \overline{c_e} q'_a) \quad (3)$$

This term captures the passive thermodynamic adjustments or damping effects from the near-surface atmospheric boundary layer, driven by perturbations in 2-meter air temperature and specific humidity.

3. Dynamic and Residual Terms:

The remaining terms encompass the Wind-driven term ($\mathrm{THF}'_{\mathrm{wind}}$), which reflects the modulation of heat exchange by mesoscale wind speed perturbations, the turbulent-transfer coefficient term ($\mathrm{THF}'_{\mathrm{TC}}$), representing variations in atmospheric stability and surface roughness, and the higher-order non-linear Residuals (RES). In our regional attribution analysis, these dynamical and non-linear terms are grouped together to contrast with the primary thermodynamic drivers.

By applying this rigorous linear decomposition framework to the decadal trends of the input variables, we can pinpoint whether the amplification of eddy-induced THF is driven from the ocean below (via $\mathrm{THF}'_{\mathrm{ocean}}$), the atmosphere above (via $\mathrm{THF}'_{\mathrm{atmos}}$), or dynamic wind modulations.

Calculation of background SST gradients and EKE

To explicitly disentangle the relative mechanistic contributions of thermodynamic forcing (frontal sharpening) and dynamic vigor (eddy intensity) to the amplification of mesoscale heat fluxes, we quantified the background SST gradients and EKE[33]. The large-scale background thermodynamic state was extracted by applying the aforementioned temporal low-pass filter to the high-resolution SST fields, effectively eliminating transient synoptic noise to yield a robust background mean state. The magnitude of the horizontal background SST gradient was subsequently computed using finite central differences across the spatial grid, defined mathematically as

$$|\nabla\overline{\mathrm{T}}| = \sqrt{(\partial\overline{\mathrm{T}}/\partial \mathrm{x})^2 + (\partial\overline{\mathrm{T}}/\partial \mathrm{y})^2} \quad (4)$$

Concurrently, to quantify the dynamic intensity of the mesoscale eddy field, expressed as

$$\mathrm{EKE} = \frac{1}{2}(\mathrm{u}'^2 + \mathrm{v}'^2) \quad (5)$$

the units of EKE are ($cm^2\ s^{-2}$), the terms u' and v' are the zonal and meridional surface geostrophic velocity anomalies which derived from the CMEMS altimetry product.

Trends, significance and confidence

Long-term trends were estimated only for grid cells in which at least 80% of the temporal samples contained valid data. For each eligible grid cell, decadal trends were calculated using the non-parametric Theil–Sen estimator[40,41]. The 90% confidence interval of the trend was derived from the Sen slope confidence interval. Statistical significance was assessed using a two-sided Mann–Kendall test[42]. To reduce the influence of serial correlation on the trend significance, trend-free pre-whitening was applied before the Mann–Kendall test[43].

Data availability

All datasets used in this study are publicly available from their respective data providers. The ERA5 reanalysis data are available from the European Centre for Medium-Range Weather Forecasts/Copernicus Climate Data Store at https://doi.org/10.24381/cds.bd0915c6[44]. The CFSR/CFSv2 data are available from the National Centers for Environmental Prediction at https://gdex.ucar.edu/. The MERRA-2 reanalysis data are available from NASA Goddard Earth Sciences Data and Information Services Center at https://disc.gsfc.nasa.gov/datasets?project=MERRA-2. The GHFD product used in this study is available from Science Data Bank at https://doi.org/10.5194/essd-2025-528 under the DOI 10.57760/sciencedb.24400[45]. The SeaFluxV3 product is available at https://www.earthdata.nasa.gov/data/catalog/ghrc-daac-seaflux-1[46]. The OHFv2 product is available at https://www.ncei.noaa.gov/products/climate-data-records/ocean-heat-fluxes. The ESA SST CCI/C3S reprocessed sea surface temperature data and Global Ocean Gridded L4 Sea Surface Heights and Derived Variables product are available at CMEMS through https://data.marine.copernicus.eu/products. The NOAA Optimum Interpolation Sea Surface Temperature product is available at https://www.ncei.noaa.gov/products/optimum-interpolation-sst. The Mesoscale Eddy Trajectory Atlas products, including the delayed-time all-satellite META3.2 product and the near-real-time META3.2 experimental product, are available from AVISO at https://www.aviso.altimetry.fr/en/data.html.

The processed data necessary to reproduce the figures and regional statistics are available from the corresponding authors upon reasonable request.

References

1. Small, R. J. et al. Air–sea interaction over ocean fronts and eddies. *Dyn. Atmospheres Oceans* 45, 274–319 (2008).
2. Seo, H. et al. Ocean mesoscale and Frontal-scale Ocean–atmosphere interactions and influence on Large-scale climate: a review. *J. Clim.* **36**, 1981–2013 (2023).
3. Czaja, A., Frankignoul, C., Minobe, S. & Vannière, B. Simulating the midlatitude atmospheric circulation: what might we gain from high-resolution modeling of air-sea interactions? *Curr. Clim. Change Rep.* **5**, 390–406 (2019).

4. Hogg, A. M. et al. Recent trends in the Southern Ocean eddy field. *J. Geophys. Res. Oceans* **120**, 257–267 (2015).
5. Skyllingstad, E. D., Vickers, D., Mahrt, L. & Samelson, R. Effects of mesoscale sea-surface temperature fronts on the marine atmospheric boundary layer. *Bound.-Layer. Meteorol.* **123**, 219–237 (2007).
6. Chelton, D. B., Schlax, M. G. & Samelson, R. M. Global observations of nonlinear mesoscale eddies. *Prog. Oceanogr.* **91**, 167–216 (2011).
7. Frenger, I., Gruber, N., Knutti, R. & Münnich, M. Imprint of Southern Ocean eddies on winds, clouds and rainfall. *Nat. Geosci*. **6**, 608–612 (2013).
8. Miyamoto, A., Nakamura, H. & Miyasaka, T. Influence of the subtropical high and storm track on low-cloud fraction and its seasonality over the south Indian Ocean. *J. Clim*. **31**, 4017–4039 (2018).
9. Yu, L. Global Air–sea fluxes of heat, fresh water, and momentum: Energy budget closure and unanswered questions. *Annu. Rev. Mar. Sci*. **11**, 227–248 (2019).
10. Intergovernmental Panel on Climate Change (IPCC). *Climate Change 2021: The Physical Science Basis. Contribution of Working Group I to the Sixth Assessment Report of the Intergovernmental Panel on Climate Change* (eds. Masson-Delmotte, V. et al.) (Cambridge Univ. Press, Cambridge, 2021).
11. Song, Q., Cornillon, P. & Hara, T. Surface wind response to oceanic fronts. *J. Geophys. Res.: Oceans* **111**, C12006 (2006).
12. Early, J. J., Samelson, R. M. & Chelton, D. B. The evolution and propagation of quasigeostrophic ocean eddies. *J. Phys. Oceanogr*. **41**, 1535–1555 (2011).
13. Li, X., Zhai, F. & Liu, Y. Study on the impact of mesoscale eddies on air-sea interface heat exchange in the tropical northwest Pacific from 1993 to 2019. *Oceanol. Limnol. Sin.* **56**, 237–251 (2025).
14. McWilliams, J. C. Submesoscale currents in the ocean. *Proc. R. Soc. A* **472**, 20160117 (2016).
15. Gaube, P., McGillicuddy, D. J., Chelton, D. B., Behrenfeld, M. J. & Strutton, P. G. Satellite observations of mesoscale eddy-induced Ekman pumping. *J. Phys. Oceanogr.* **44**, 2062–2076 (2014).
16. Chelton, D. B. & Xie, S.-P. Coupled ocean–atmosphere interaction at oceanic mesoscales. *Oceanography* **23**, 52–69 (2010).
17. Small, R. J. et al. Air–sea turbulent heat fluxes in climate models and observational analyses. *J. Clim*. **32**, 6289–6310 (2019).
18. Liu, Y., Yu, L. & Chen, G. Characterization of sea surface temperature and air-sea heat flux anomalies associated with mesoscale eddies in the South China Sea. J. Geophys. *Res.: Oceans* **125**, e2019JC015470 (2020).
19. Aguedjou, H. M. A. et al. Imprint of mesoscale eddies on air–sea interaction in the tropical Atlantic Ocean. *Remote Sens.* **15**, 3087 (2023).
20. Ma, X. et al. Western boundary currents regulated by interaction between ocean eddies and the atmosphere. *Nature* **535**, 533–537 (2016).
21. Phillips, H. E. & Rintoul, S. R. Eddy variability and energetics from direct current measurements in the Antarctic Circumpolar Current south of Australia. *J. Phys. Oceanogr.* **30**, 3050–3076 (2000).

22. Qiu, B. & Chen, S. Variability of the Kuroshio Extension jet, recirculation gyre, and mesoscale eddies on decadal time scales. *J. Phys. Oceanogr.* **35**, 2090–2103 (2005).
23. Sutton, R. & Dong, B. Atlantic Ocean influence on a shift in European climate in the 1990s. *Nat. Geosci.* **5**, 788–792 (2012).
24. Freeman, N. M., Lovenduski, N. S. & Gent, P. R. Temporal variability in the Antarctic Polar Front (2002–2014). *J. Geophys. Res.: Oceans* **121**, 7263–7276 (2016).
25. Leyba, I. M., Saraceno, M. & Solman, S. A. Air–sea heat fluxes associated with mesoscale eddies in the southwestern Atlantic Ocean and their dependence on different regional conditions. *Clim. Dyn.* **49**, 2491–2501 (2017).
26. Zhang, N., Lan, J., Yu, Y., Zhang, Y. & He, Y. Seasonal variations in Eddy-Induced atmospheric perturbations in the South China Sea. *J. Clim*. **37**, 551–567 (2024).
27. Qu, Y., Wang, S., Jing, Z., Wang, H. & Wu, L. Spatial structure of vertical motions and associated heat flux induced by mesoscale eddies in the upper Kuroshio–Oyashio Extension. *J. Geophys. Res.: Oceans* **127**, e2022JC018781 (2022).
28. Ma, X. et al. Midlatitude mesoscale thermal air-sea interaction enhanced by greenhouse warming. *Nat. Commun.* **15**, 7699 (2024).
29. Tang, R. et al. A review of global products of air–sea turbulent heat flux: accuracy, mean, variability, and trend. *Earth-Sci. Rev.* **249**, 104662 (2024).
30. Buck, A. L. New equations for computing vapor pressure and enhancement factor. *J. Appl. Meteorol.* **20**, 1527–1532 (1981).
31. Chelton, D. B., Schlax, M. G. & Freilich, M. H. Satellite measurements reveal persistent small-scale features in ocean winds. *Science* **303**, 978–983 (2004).
32. O'Neill, L. W., Chelton, D. B. & Esbensen, S. K. The effects of SST-induced surface wind speed and direction on midlatitude air–sea interaction. *J. Clim.* **23**, 591–613 (2010).
33. Martínez-Moreno, J. et al. Global changes in oceanic mesoscale currents over the satellite altimetry record. *Nat. Clim. Chang.* **11**, 397–403 (2021).
34. Ferrari, R. & Nikurashin, M. Suppression of eddy diffusivity across jets in the Southern Ocean. *Prog. Oceanogr.* **84**, 60–72 (2010).
35. Abernathey, R. & Marshall, J. Global surface eddy diffusivities derived from satellite altimetry. *J. Phys. Oceanogr.* **43**, 1790–1804 (2013).
36. Wu, L. et al. Enhanced warming over the global subtropical western boundary currents. *Nat. Clim. Chang.* **2**, 161–166 (2012).
37. Thompson, D. W. J. & Solomon, S. Interpretation of recent Southern Hemisphere climate change. *Science* **296**, 895–899 (2002).
38. Yang, H. et al. Intensification and poleward shift of western boundary currents under global warming. *Nat. Clim. Chang.* **6**, 547–552 (2016).
39. Bôas, A. B. V., Sato, O. T., Chaigneau, A. & Castelão, G. P. The signature of mesoscale eddies on the air–sea turbulent heat fluxes in the South Atlantic Ocean. *Geophys. Res. Lett.* **42**, 1856–1862 (2015).
40. Sen, P. K. Estimates of the regression coefficient based on Kendall's tau. *J. Am. Stat. Assoc*. **63**, 1379–1389 (1968).

41. Theil, H. A rank-invariant method of linear and polynomial regression analysis. *Proc. K. Ned. Akad. Wet*. **53**, 386–392 (1950).
42. Yue, S. & Wang, C. The Mann–Kendall test modified by effective sample size to detect trend in serially correlated hydrological series. *Water Res. Manage*. **18**, 201–218 (2004).
43. Yue, S., Pilon, P., Phinney, B. & Cavadias, G. The influence of autocorrelation on the ability to detect trend in hydrological series. *Hydrol. Process.* **16**, 1807–1829 (2002).
44. Faghmous, J. H., Le, M., Uluyol, M., Kumar, V. & Chatterjee, S. A parameter-free spatio-temporal pattern mining model to catalog global ocean dynamics. In *2013 IEEE 13th International Conference on Data Mining* 151–160 (IEEE, Dallas, TX, 2013).
45. Peng, W., Ma, Z., Zhang, D., Ye, H. & Fei, J. A Global Surface Turbulence Heat Flux Dataset resolving tropical cyclones. Preprint at *Earth Syst. Sci. Data Discuss.* Preprint at https://doi.org/10.5194/essd-2025-528 (2025).
46. Roberts, J. B. & Clayson, C. A. *SeaFlux Data Products*. NASA Global Hydrometeorology Resource Center Distributed Active Archive Center, https://doi.org/10.5067/SEAFLUX/DATA101 (2025).

Acknowledgements

This work was supported by the National Key Research and Development Program of China (Grant No. 2022YFF0801400), the Shandong Provincial Natural Science Foundation (Grant No. ZR2024LQX002), and the National Science Foundation of China (Grant No. 42276010).

Author information

Authors and Affiliations

State Key Laboratory of Physical Oceanography, College of Oceanic and Atmospheric Sciences, Ocean University of China, Qingdao, China

Yikuan Liu, Fangguo Zhai, Zizhou Liu

Hebei Key Laboratory of Ocean Dynamics, Resources and Environments, Qinhuangdao, China

Fangguo Zhai

Key Laboratory of Marine Environment and Ecology, College of Environmental Science and Engineering, Ocean University of China, Qingdao, China

Xiaojie Yu

Hainan Institute of Zhejiang University, Sanya, China

Cong Liu

State Key Laboratory of Ocean Sensing & Ocean College, Zhejiang University, Zhoushan, China

Yanzhen Gu, Peiliang Li

Corresponding authors

Correspondence to Fangguo Zhai (gfzhai@ouc.edu.cn) & Xiaojie Yu (yxj@ouc.edu.cn)

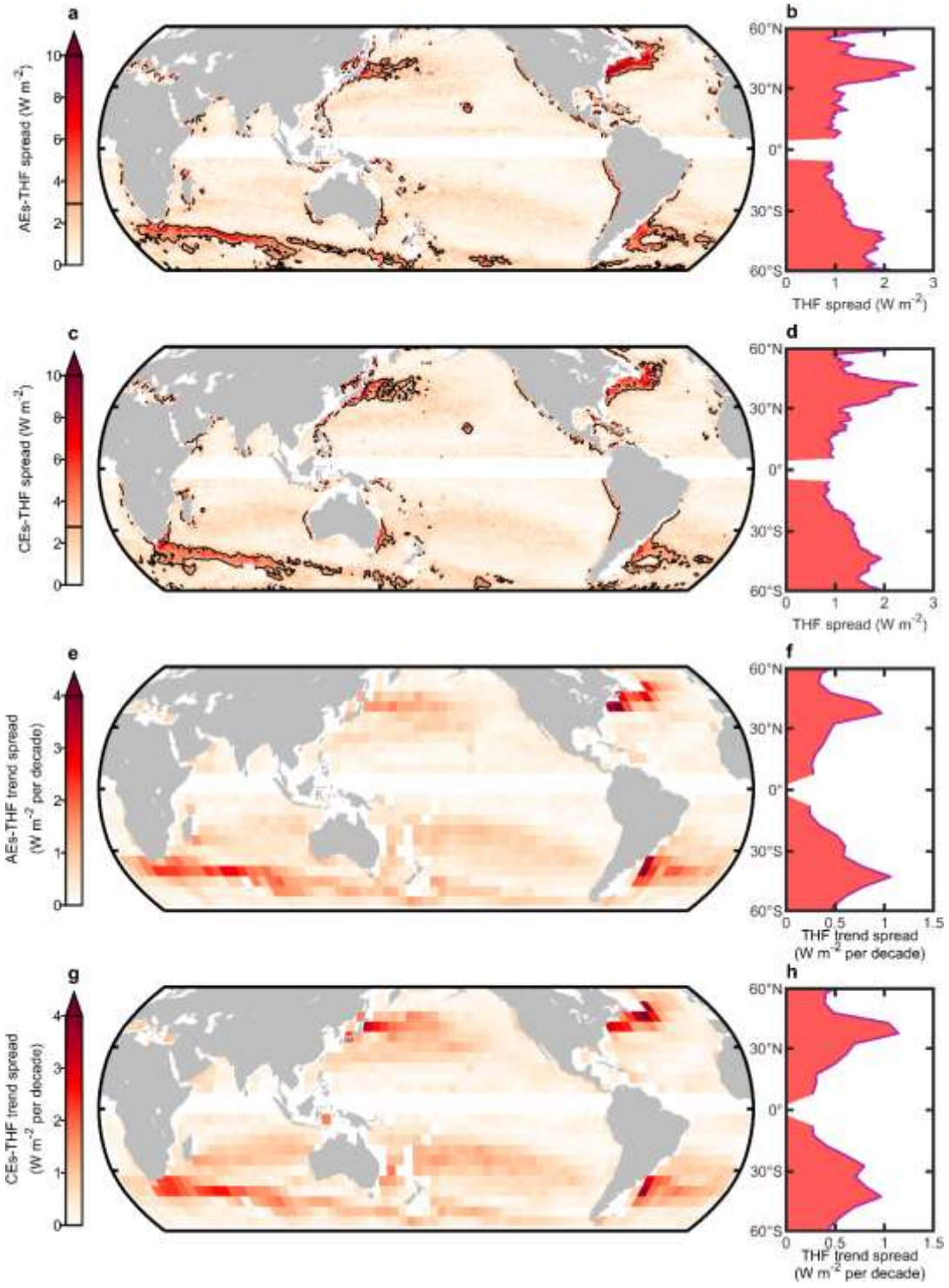
Author contributions

Y.L. and F.Z. conceived the study. Y.L. performed the analysis and prepared the figures. Y.L. wrote the initial manuscript with input from F.Z. and X.Y. All authors discussed the results and contributed to the final manuscript.

Competing interests

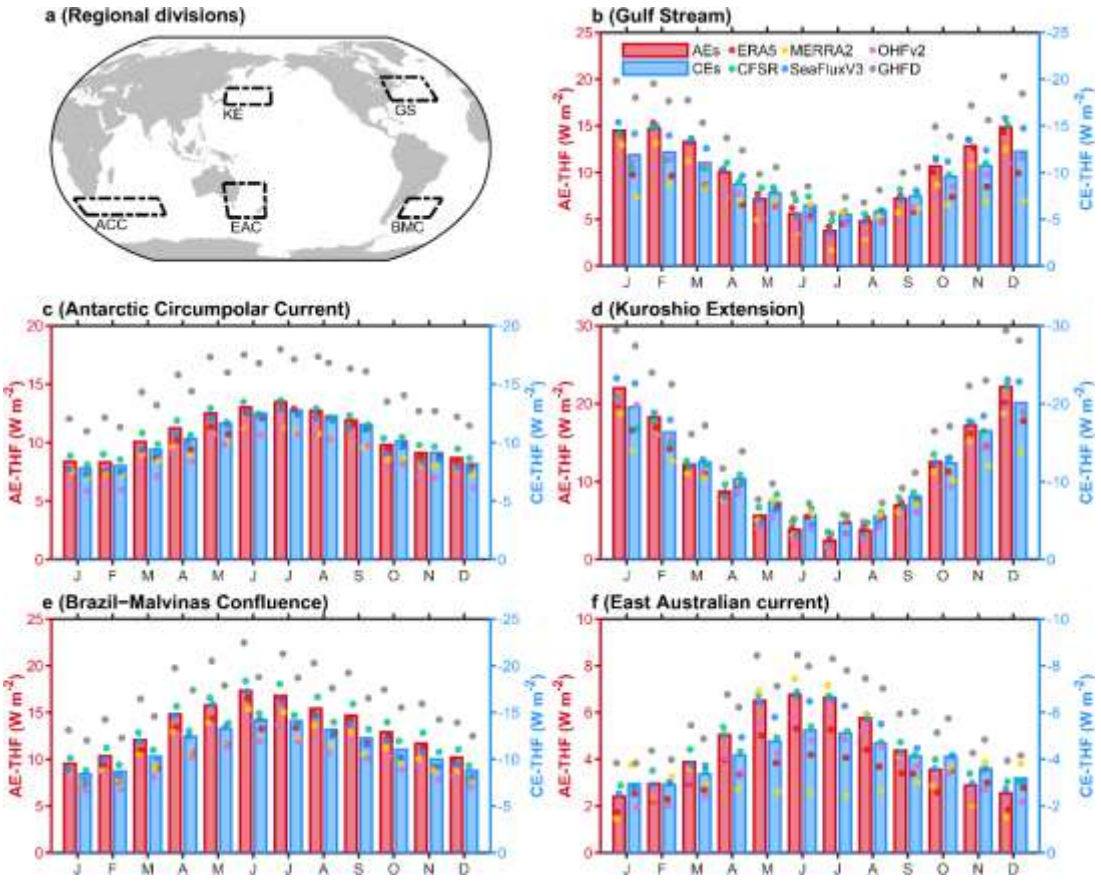
The authors declare no competing interests.

Extended Data Figures



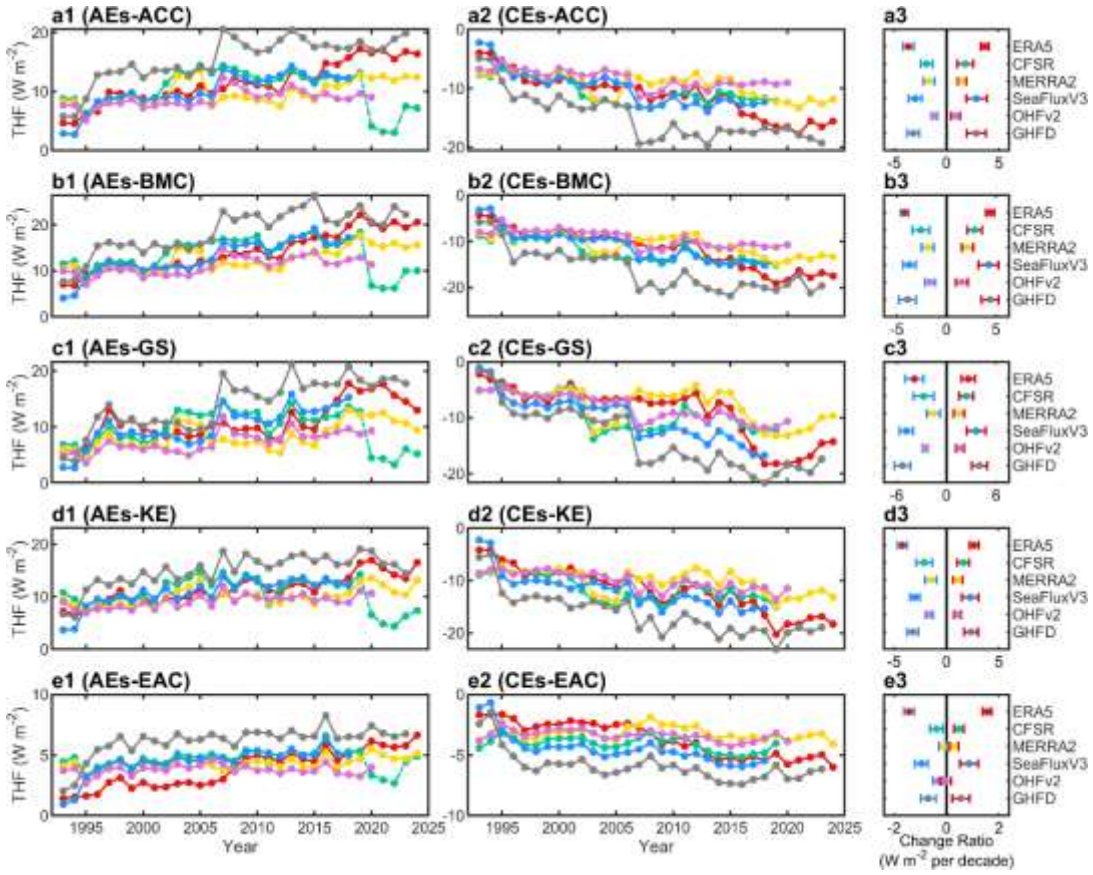
Extended Data Fig. 1 | Inter-product spread in climatological eddy-induced THF anomalies and their decadal trends between 1993 and 2018. **a, c**, Global spatial distributions of the eddy-induced THF anomalies spread (W m^{-2}) for AEs (**a**) and CEs (**c**). **b, d**, Corresponding zonal mean profiles of the THF spread for AEs (**b**) and CEs (**d**). **e, g**, Global spatial distributions of the inter-product spread in decadal trends of eddy-induced THF (W m^{-2} per decade) for AEs (**e**) and CEs (**g**). **f, h**, Corresponding zonal mean profiles of the inter-product spread in AE- and CE-

induced THF trends. The spread is calculated as the inter-product standard deviation across six independent air–sea flux datasets: ERA5, CFSR, MERRA2, SeaFluxV3, OHFv2 and GHFD.



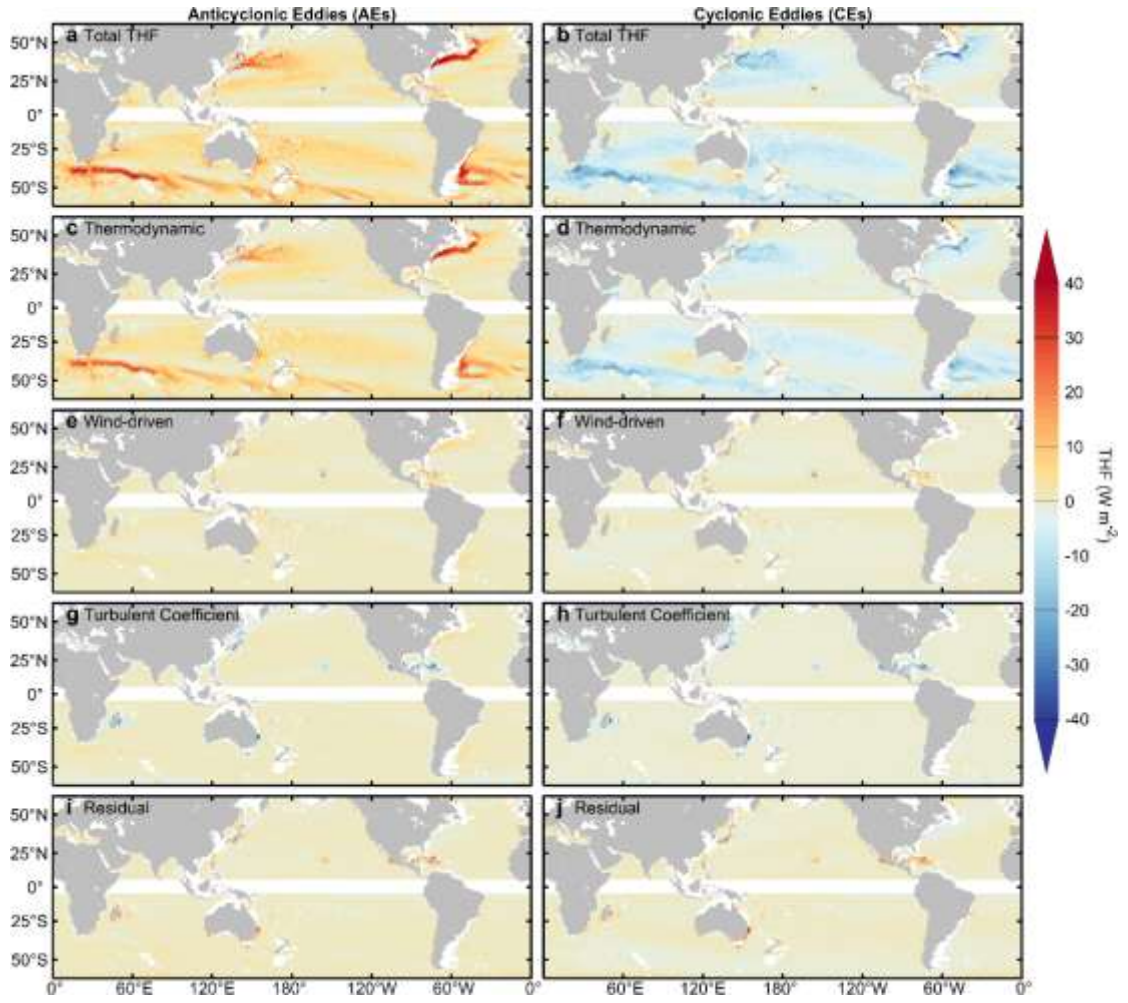
Extended Data Fig. 2 | Regional divisions and monthly variations of eddy-induced THF intensity.

a, Schematic map indicating the five selected study regions outlined by black dashed boxes: ACC, KE, GS, EAC and BMC. **b–f**, Monthly climatology of eddy-induced THF intensity across the (**b**) ACC, (**c**) BMC, (**d**) GS, (**e**) KE, and (f) East Australian Current. Red bars denote the THF intensity induced by anticyclonic eddies (AE-THF, left y-axis), while blue bars represent the THF intensity induced by cyclonic eddies (CE-THF, right y-axis). The overlaid scatter points indicate the specific intensity values derived from six individual datasets (ERA5, CFSR, MERRA2, SeaFluxV3, OHFv2, and GHFD). Units are in W m^{-2}.



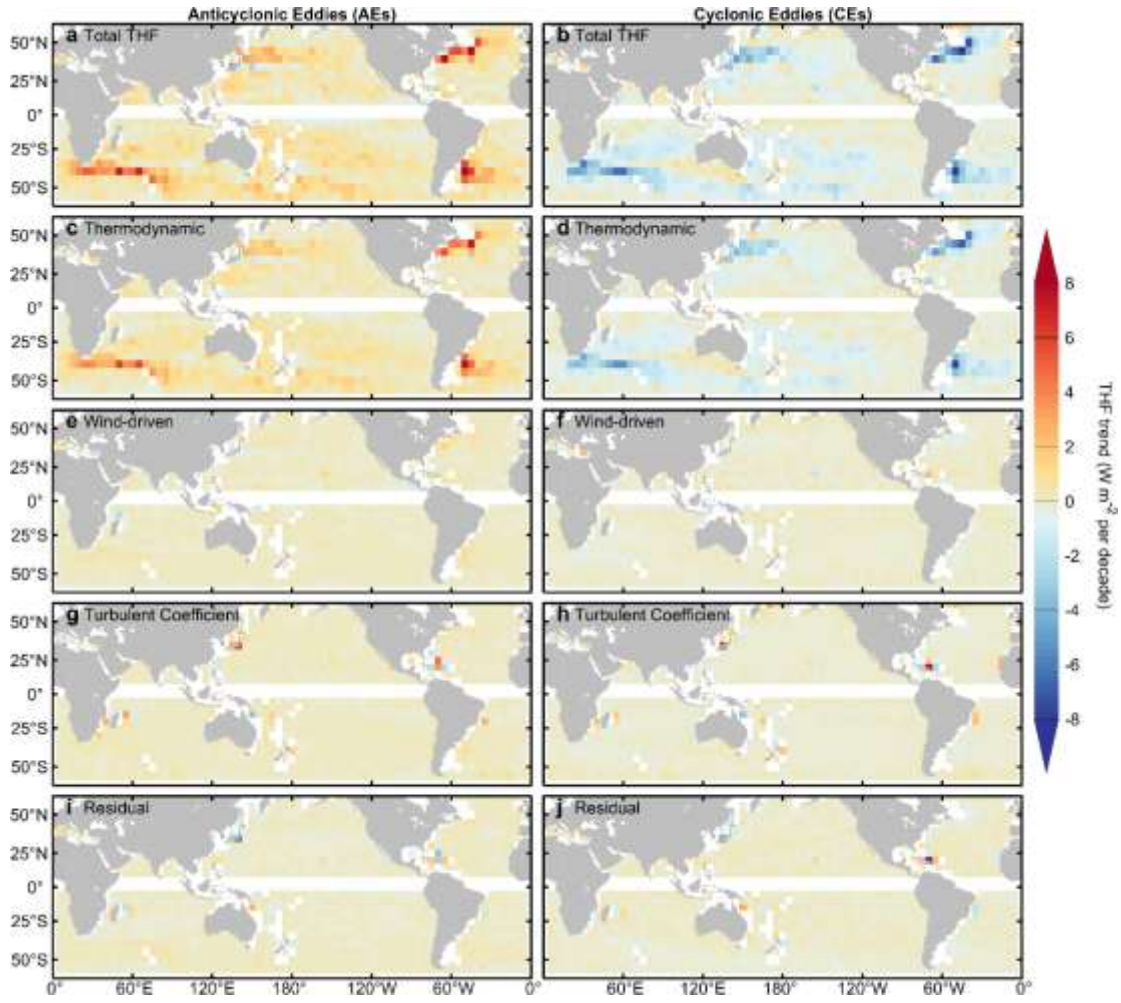
Extended Data Fig. 3 | Annual time series and decadal trends of eddy-induced THF intensity.

a1–e1, Interannual variations of THF intensity induced by AEs across five key oceanic regions: ACC (**a1**), BMC (**b1**), GS (**c1**), KE (**d1**), and EAC (**e1**). The various colored lines represent the evaluations from six distinct datasets (ERA5, CFSR, MERRA2, SeaFluxV3, OHFv2, and GHFD). **a2–e2**, Corresponding annual time series of THF intensity induced by CEs for the same regions. **a3–e3**, Decadal trends (Change Ratio, in W m^{-2} per decade) and their corresponding CIs for AE-THF (red markers) and CE-THF (blue markers) across the six datasets. All trends and CIs are estimated using the Theil–Sen method.



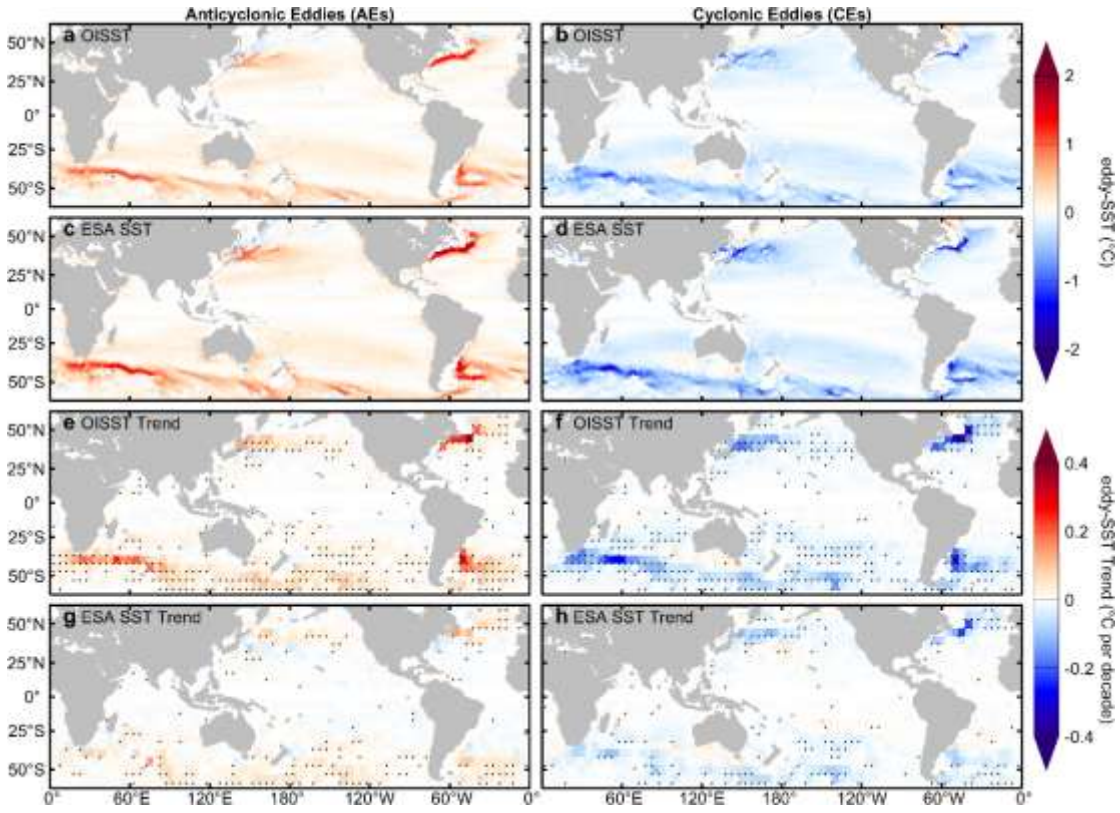
Extended Data Fig. 4 | Linearized thermodynamic decomposition of THF from CFSR between 1993 and 2018.

a, c, e, g, i, Global spatial distributions of the total AE-induced THF (**a**) and its decomposed constituent components based on a linearized perturbation approximation: the gradient-driven term (**c**), the wind-driven term (**e**), the turbulent-transfer coefficient term (**g**), and the residual terms (higher-order non-linear residual terms; **i**). **b, d, f, h, j**, Corresponding distributions for CEs and their respective decomposed terms. All attributions are derived from the CFSR dataset.



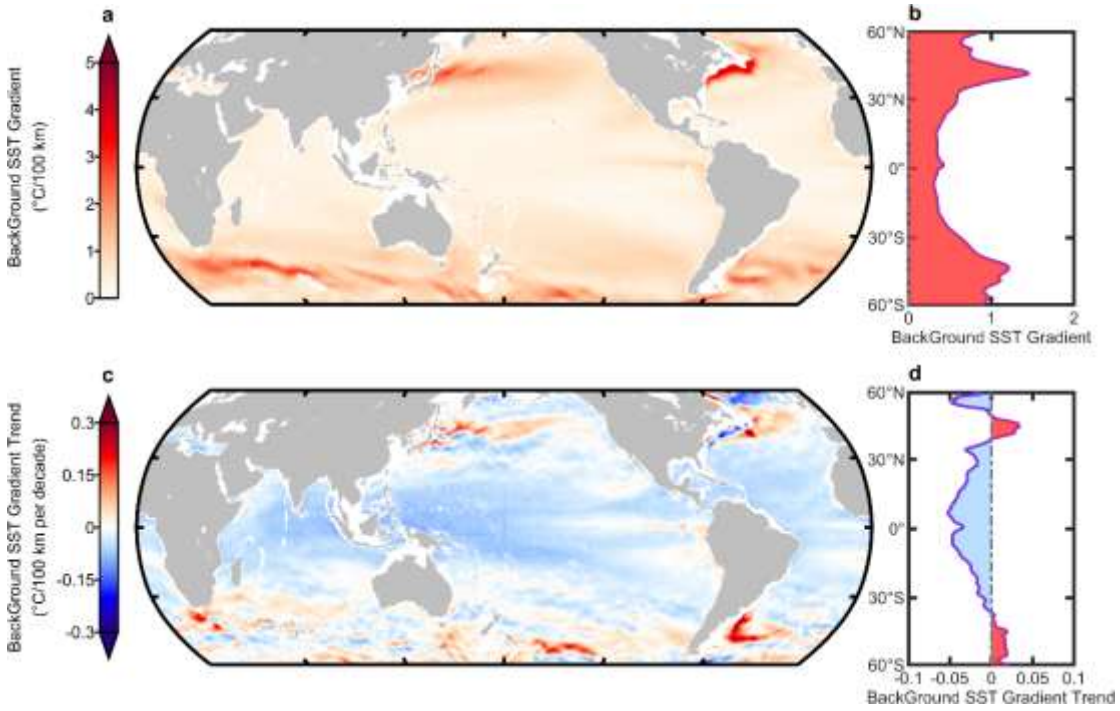
Extended Data Fig. 5 | Thermodynamic attribution of the long-term trend in eddy-induced THF between 1993 and 2018.

a, c, e, g, i, Global spatial distributions of decadal trends (W m^{-2} per decade) in the total AE-induced THF (**a**) and its decomposed constituent components based on a linearized perturbation approximation: the gradient-driven term (**c**), the wind-driven term (**e**), the turbulent-transfer coefficient term (**g**), and the residual terms (**i**). **b, d, f, h, j**, Corresponding decadal trends for CEs and their respective decomposed terms. All attributions are derived from the CFSR dataset.



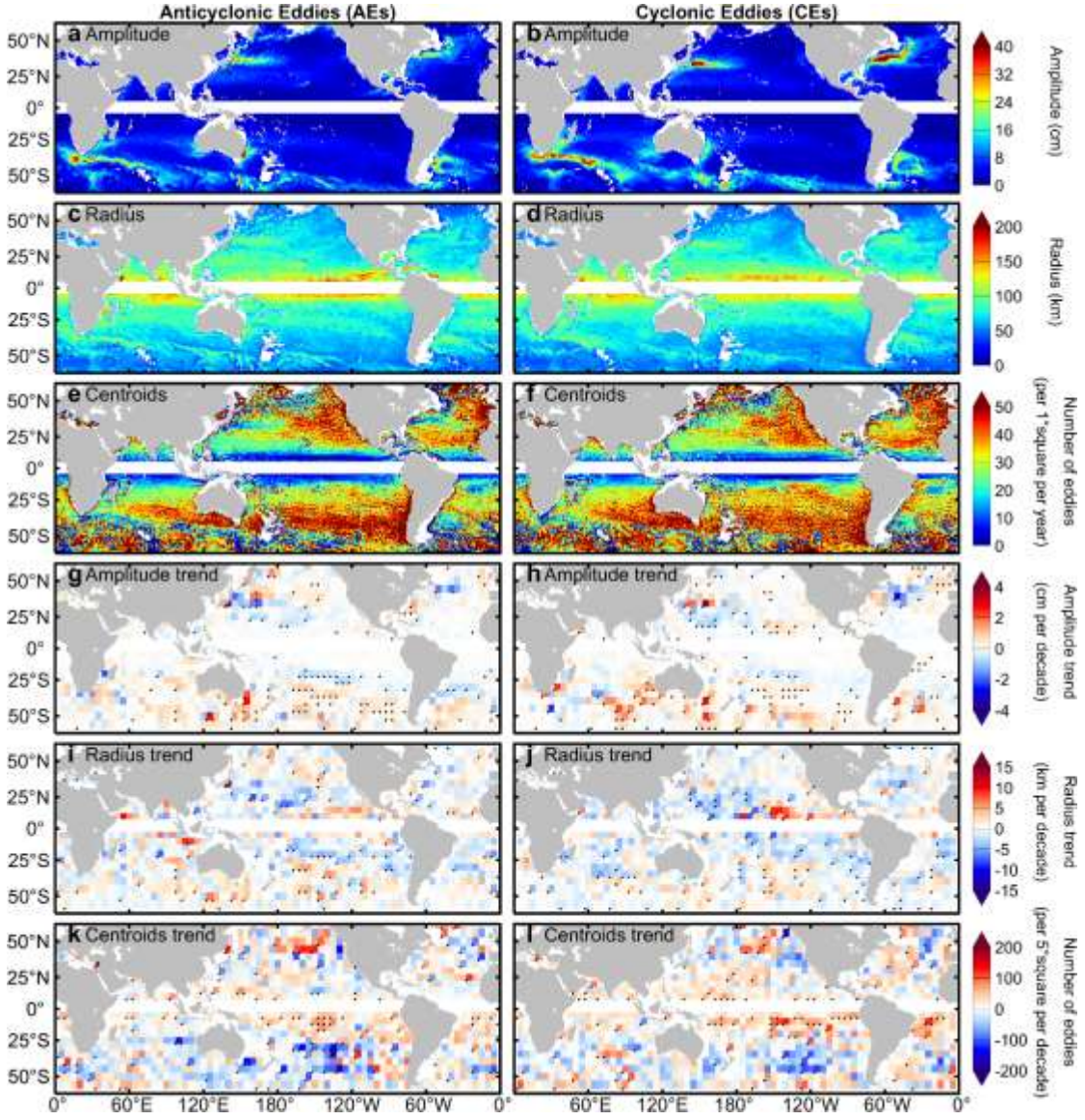
715

716 **Extended Data Fig. 6 | Climatological mean and decadal trends of eddy-induced**
717 **SST between 1993 and 2018.**
718 **a-d**, Global spatial distribution of the climatological mean eddy-induced SST anomalies
719 (°C) for AEs (**a**, **c**) and CEs (**b**, **d**), derived from OISST (**a**, **b**) and ESA SST (**c**, **d**)
720 datasets. **e–h**, Corresponding decadal trends in the magnitude of eddy-induced SST
721 anomalies (°C per decade) for AEs (**e**, **g**) and CEs (**f**, **h**), black dots indicate regions are
722 statistically significant above the 95% confidence level.



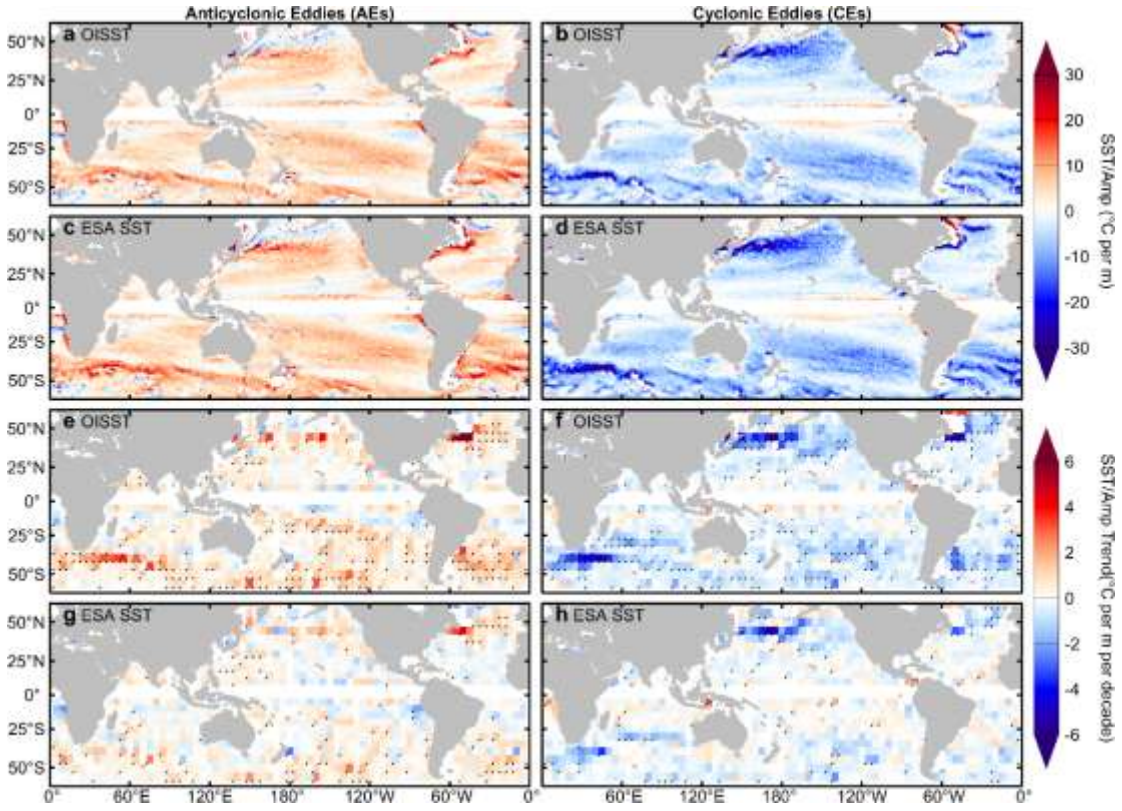
723

Extended Data Fig. 7 | mean SST gradient magnitude and SST gradient magnitude trends between 1993 and 2018 calculated using OISST.
a, **b**, Global spatial distribution (**a**) and the corresponding zonal mean profile (**b**) of the climatological background SST gradient (°C/100 km). **c**, **d**, Global spatial distribution (**c**) and the zonal mean profile (**d**) of the decadal trend in the background SST gradient (°C/100 km per decade). Positive trends (red shading) indicate a widespread intensifying, or sharpening, of the background thermal fronts.

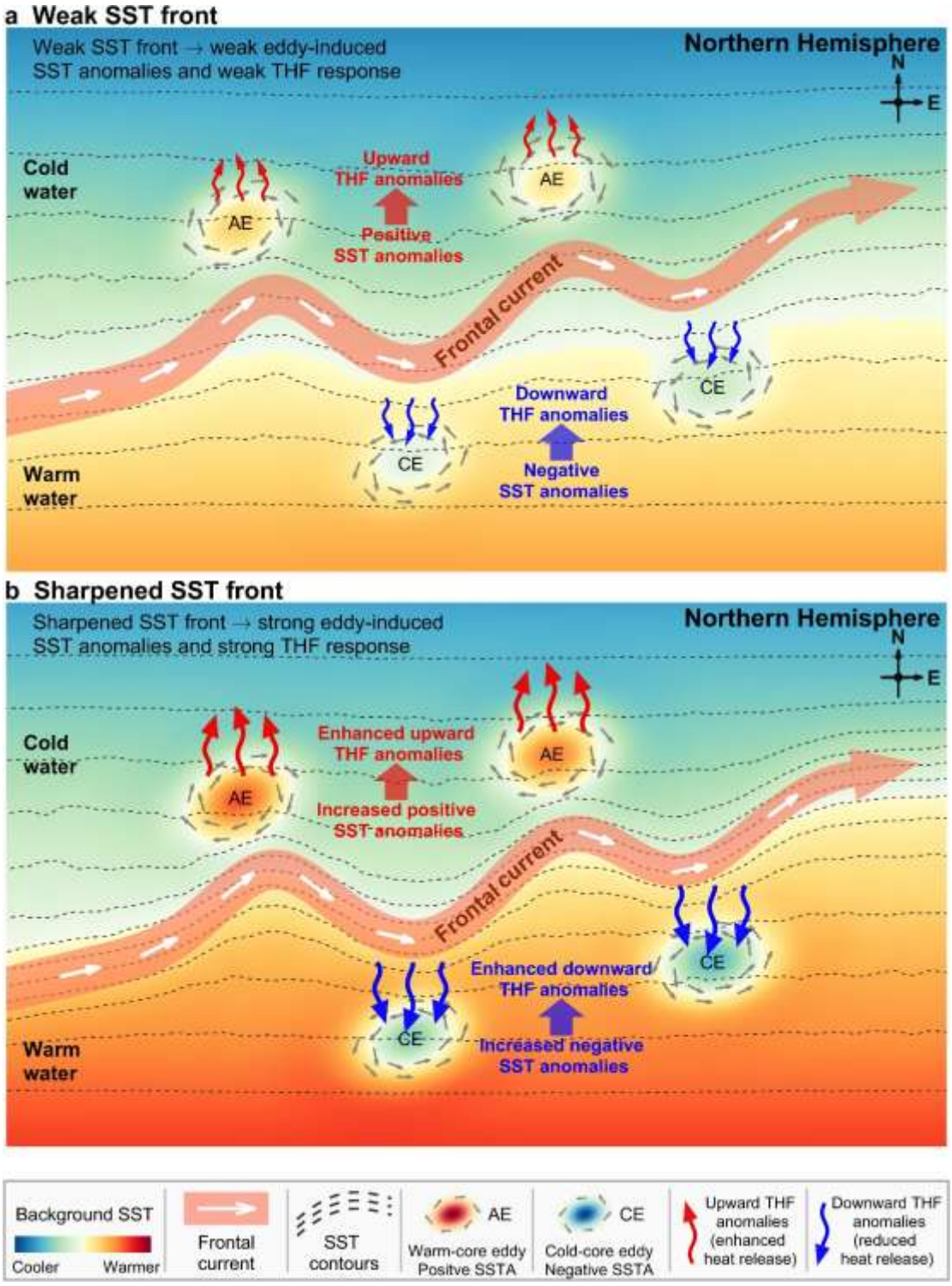


Extended Data Fig. 8 | Climatological spatial distributions and decadal trends of eddy amplitude, radius and the numbers of eddy centroids between 1993 and 2018.
a, **b**, Spatial distributions of the climatological mean amplitude (cm) of AEs (**a**) and CEs (**b**). **c**, **d**, Same as a and b, but for the climatological mean eddy radius (km). **e**, **f**, Spatial distributions of eddy centroid counts for AEs (**e**) and CEs (**f**), calculated within each 1° × 1° grid cell. g, h, Decadal trends in eddy amplitude (cm per decade) for AEs (g) and CEs (h), calculated within each 5° × 5° grid cell. **i, j**, Same as g and h, but for trends in eddy radius (km per decade). **k, l**, Decadal trends in eddy centroid counts (per 5° × 5° grid cell per decade) for AEs (**k**) and CEs (**l**), calculated within each 5° × 5°

grid cell. Trends are estimated using the Theil–Sen method, and black stippling denotes regions where the trends are statistically significant at the 95% confidence level based on the Mann–Kendall test. Eddy amplitude, radius and centroid counts are derived from the global mesoscale eddy trajectory dataset.



Extended Data Fig. 9 | Climatological mean and decadal trends of amplitude-normalized eddy-induced SST anomalies between 1993 and 2018.
a-d, Spatial distribution of normalized eddy-induced SST anomalies (°C per m) for AEs (**a**, **c**) and CEs (**b**, **d**), derived from OISST (**a**, **b**) and ESA SST (**c**, **d**). **e–h**, Corresponding decadal trends of normalized eddy-induced SST anomalies (°C per m per decade) for AEs (**e**, **g**) and CEs (**f**, **h**), black dots indicate regions are statistically significant above the 95% confidence level.



Extended Data Fig. 10 | Conceptual schematic illustrating how sharpened background SST fronts amplify eddy-induced SST anomalies and THF responses. **a**, Under a weak frontal background, the meridional SST gradient across the frontal current is relatively weak. AEs and CEs detached from or embedded within the frontal zone generate only modest warm-core and cold-core SST anomalies, respectively. Consequently, AEs generate upward THF anomalies (enhanced ocean-to-atmosphere turbulent heat release), whereas CEs generate downward THF anomalies (reduced the ocean-to-atmosphere heat release). **b**, sharpened SST gradients provide a larger

763 thermodynamic contrast for mesoscale eddies. For comparable eddy perturbations, AEs
764 induce stronger positive SST anomalies and CEs induce stronger negative SST
765 anomalies, thereby producing amplified turbulent heat flux responses: enhanced
766 upward heat flux over warm-core AEs and stronger downward THF anomalies over
767 cold-core CEs.
768
769
770
771

Supplementary Files

This is a list of supplementary files associated with this preprint. Click to download.

- SupplementaryInformation.docx